LINEAR VERSUS NONLINEAR FILTERING OF SIGNAL DEPENDENT IMAGE NOISE

by

CHINTANIE P. WETTASINGHE, B.S.

A THESIS

IN

ELECTRICAL ENGINEERING

Submitted to the Graduate Faculty
of Texas Tech University in
Partial Fulfillment of
the Requirements for
the Degree of

MASTER OF SCIENCE

IN

ELECTRICAL ENGINEERING

Approved

August, 1996

ACKNOWLEDGEMENT

This thesis is dedicated to my parents for opening up worlds to me. Their encouragement, guidance, and loving support have always inspired me to extend my limits. I will ever be indebted to them for all the sacrifices they have made in their lives to give me bigger and better opportunities.

I would like to express my sincere appreciation to Dr. Sunanda Mitra for her guidance and support throughout this research. She accepted me at a time when I was at loose ends, and guided me in a new direction to achieve my goals, for which I will ever be grateful. Deep appreciation is also extended to Dr. Thomas Krile and Dr. Kwong Shu Chao for their valuable insight of this thesis.

Finally, I would like to thank all my friends in the Department of Electrical Engineering for their generous help during my graduate study here at Texas Tech University.

TABLE OF CONTENTS

CHAPTER

ABSTRACT

Digital images are degraded by noise either during image acquisition or during image transmission, or both. One of the primary concerns of digital image processing is to reduce this noise for optimal recovery of the original image from a degraded copy. The purpose of this research is to investigate the restoration of images corrupted by signal dependent noise using linear and nonlinear filtering techniques. The type of noise considered in this study is speckle noise which occurs in all types of coherent imaging systems. The linear filtering technique employed here is multiresolution wavelet decomposition of a noisy image and reconstruction of the image by discarding selective detail images at each level of decomposition. We studied this technique by varying the choice of number of wavelet coefficients, and using a synthetic aperture radar (SAR) image and an ultrasound medical image with simulated speckle noise. It was observed that this technique removed the speckle noise of the images appreciably, but caused severe blurring of edges and other sharp details important to them. When the same images were used, the conventional nonlinear median filter removed noise significantly. However, it destroyed some fractal details of the images. A recently developed connectivity preserving morphological filter which is also of the nonlinear type provided the best restoration of images degraded with speckle noise. We characterized the performance of the wavelet, median and morphological filters by using criteria such as visual fidelity, mean square error (MSE), normalized mean square error (NMSE), peak signal-to-noise ratio (PSNR), and intensity profile analysis.

LIST OF TABLES

LIST OF FIGURES

CHAPTER 1

INTRODUCTION

The presence of noise in digital images is a fundamental problem in many image processing applications, as the noise tends to alter the quality of images considerably. Any image is likely to be degraded by some type of noise which may originate in the image formation process, the transmission medium, the recording process or any combination of these [1]. Therefore, noise reduction is an image restoration problem that has been studied for many years to obtain an optimal approximation of the original image from the degraded observations.

1.1 Signal Dependent Noise in Images

When photographic film is used as the detection-recording mechanism, noise, called film-grain noise, is introduced [2]. This is mainly due to the grains of silver that compose the developed image. When photoelectronic systems are used for image detection and recording, there are two kinds of noise that originate; photoelectron noise and thermal noise [3]. The former is produced by random fluctuations of the number of photons and photoelectrons on the light-sensitive surface of the detector. The sources of the latter are the various electronic circuits that sense, acquire, and process the signal from the detector's photorefractive surface [1]. Another type of noise that occurs in coherent imaging of objects is called speckle noise. In this study, we have primarily addressed the issue of images corrupted by speckle noise.

All the above types of noise except thermal noise are signal-dependent in nature [3]. In the formation of images, the type of noise generated is mostly signal dependent. It is frequently multiplicative, and nonlinearly related to the strength of the "signal" (ideal image).

1.2 Speckle Noise in Images

Speckle is a type of noise that is commonly encountered in real world images. It occurs in all types of coherent imagery, such as synthetic aperture radar (SAR) imagery, acoustic imagery, and laser illuminated imagery [4]. When monochromatic radiation is scattered from a surface whose roughness is of the order of a wavelength, the interference of the waves produces speckle noise [5].

Speckle noise reduces the ability of a human observer to resolve fine details within an image. Speckle in medical ultrasonic images tends to mask the presence of low-contrast lesions [6], and therefore, possesses a threat to the accuracy of medical diagnostic technology. In optical radar systems, speckle can reduce the probability of target detection [7]. Speckle patterns, according to the principles of statistical optics, are noise-carrier images [8], and another one of their disadvantages is low signal-to-noise ratio (SNR). Also, the presence of any type of noise including speckle can reduce the efficiency of image compression schemes. Transform coding schemes, notably Joint Photographic Experts Group standard (JPEG) [9] can use quite a lot of storage space to code the noise in an image. That is, a noisy version of a clean image compresses to a larger size than the clean version [10,11].

1.3 The Techniques Used in Speckle Noise Reduction

Speckle noise, the "remarkable granular or peppery nature not present in ordinary light" which J. D. Rigden and E. I. Gordon first observed in 1962 [12], was quickly recognized as being a major objection to the use of coherent light. Consequently, soon after the discovery of this phenomenon, methods were sought by which it might be reduced, at least partially, if not completely. Today, there are numerous ways to deal with the problem of speckle. Basically, they all fall into two main categories [13] namely, pre-image forming and post-image forming noise reduction categories.

In the first category, the visual quality of an image is improved by averaging uncorrelated images that result from non-overlapping spectra [13]. This spatial averaging is done based on the intensities of the images. The signal-to-noise ratio (SNR) of fully developed speckle is equal to one, and the spatial averaging process is known to increase the SNR from one to $M^{1/2}$, where M is the number of uncorrelated speckled images [4]. However, this method calls for the formation of serial images and gives rise to a problem when these images have to be displayed in a real-time format [7]. Then, either image size has to be reduced or the image display rate has to be slowed down. Also, this method accompanies a loss of resolution of the image [5].

The second category comprises techniques that smooth speckles after the image has been formed. Some of the restoration techniques in this category include gray scale modification, homomorphic filtering, and lowpass filtering [7,11]. However, these techniques have a tendency to suppress the signal as well as its speckles and hence should be employed with special care.

1.4 The Problem Statement

Ever since the discovery of speckle noise, realizing the best restoration technique for images corrupted by this signal dependent type of noise has been an ongoing effort. The images that are degraded by speckle represent a very difficult and demanding application area for noise reduction algorithms [6]. Although they are heavily corrupted by noise, they possess sharp contrast which should be retained. In addition, they contain a variety of features which should also be preserved.

The development of many image restoration techniques over the years has given rise to the dilemma of deciding which method is most suitable for speckle noise reduction. Thus, the main objective of this study is to investigate the restoration of images degraded by speckle noise by employing linear and nonlinear filtering techniques. By comparing the performance of different techniques, the most suitable one to reduce speckle noise can be decided upon.

The linear filtering technique we have studied in this work is multiresolution wavelet decomposition of a noisy image and reconstruction of the image by discarding selective detail images at each level of decomposition. Wavelets decompose signals and images into multiscale details. Sharp transitions in images are preserved and depicted extremely well in wavelet expansions [14]. This special treatment of edges by wavelet transforms is very attractive in image filtering.

Among the several nonlinear filtering algorithms available in the image processing community, the median filter is probably the most popular technique [6]. It has been widely applied in many areas of image restoration because of its edge preserving properties and simplicity in implementation. In our study, we have analyzed the performance of median filtering in restoring speckled images.

Another type of a nonlinear filtering technique we have used in this study is recently developed connectivity preserving morphological filters [15]. This technique uses two new operations called bounded opening and bounded closing to effectively remove the noise spots. The commonly used morphological operations are based on convex structuring elements and hence they tend to probe regions from their interior. Bounded opening and closing on the other hand attempt to probe the tiny white and black spots, respectively from their exterior. The "speckled" or spot-like nature of the noise agrees with morphological modeling of noise.

1.5 Computer Simulation of Noisy Images

The images we have used in the simulations of our work were monochrome with pixel gray level values between 0 and 255 (8 bits). We have analyzed original SAR images and ultrasonic medical images. The ultrasonic images were corrupted with simulated speckle noise using a noise model. During the simulation of the noisy images, all pixel values generated above 255 were thresholded to 255 and all pixel values below 0 were thresholded to 0.

1.6 Thesis Outline

This thesis examines and compares the performances of linear and nonlinear filtering techniques in restoration of images corrupted by signal dependent noise, namely speckle. The linear filter chosen here is a wavelet transform-based filter, and the nonlinear ones are median and morphological filters. The organization of our work is as follows. Chapter 2 explains how speckle is produced in imaging systems. Also, it describes a speckle noise model that has been used in some of the simulations of our work. Chapter 3 looks into the mathematical properties of the wavelet transform and shows how that wavelet-based filtering technique is implemented. Chapter 4 gives a brief introduction to morphological operations and describes the new connectivity preserving filtering algorithm designed together with alternating sequential filtering (ASF). It also describes the median filtering technique we have employed in our work. Chapter 5 explains the performance criteria used to evaluate the wavelet, median, and morphological filtering techniques. Chapter 6 presents the results and discussions of our research. Finally, Chapter 7 summarizes the research and discusses possible future work.

CHAPTER 2

SPECKLE NOISE

This thesis concentrates on the performance of different restoration techniques on images degraded by speckle noise. Hence, it is of importance to understand the nature and the origin of speckle in order to deal with it successfully. Section 2.1 briefly discusses the origin of speckle in images and some of its properties.

The two sets of images that were used in our study are synthetic aperture radar (SAR) and ultrasonogram images. In the case of ultrasonograms, a noise model was used to introduce some speckle noise to the original image in order to intensify the degradation caused by noise. This facilitates the feasibility to measure the quality of the restoration (filtering) techniques that were employed in this study. Therefore, in the case of ultrasonograms, the validity and the effectiveness of the restoration techniques largely lie on the noise model assumed. In section 2.2, the speckle noise model used in this work is presented.

2.1 The Origin of Speckle

The early workers in the field of lasers noticed a peculiar granular appearance when objects were viewed in highly coherent light. They further noticed that this granularity bore no direct relationship to the macroscopic properties of the illuminated object [16]. As soon as this chaotic and unordered pattern was observed, it was then recognized as speckle. A speckle pattern is a result of a random intensity distribution of light and can arise either from an imaging operation or from free-space propagation.

In the case of an image operation, speckle noise arises from random variations in object surface roughness. The surfaces of most objects are extremely rough compared to the optical wavelength which is approximately equal to $5x10^{-7}$ meters [16]. When nearly monochromatic light is reflected from a surface with roughness of the order of a wavelength, the optical wave generated at any moderately distant point consists of many coherent components or wavelets, each arising from a different microscopic element of the surface. The distances traveled by these numerous wavelets may differ by several or many wavelengths if the surface is truly rough. These dephased but coherent wavelets interfere with each other randomly and create the granular pattern of intensity called speckle.

Speckle also occurs when fairly coherent light propagates through a medium with random refractive index fluctuations. This situation primarily occurs in astronomy because of atmospheric turbulence [16]. Speckle is then formed by random phase variations of the wavefront originating from each source point.

Speckle noise is found in all types of coherent imagery, including radar astronomy, synthetic aperture radar, and acoustical imagery. This study concentrates on SAR and ultrasonic images, and speckle in these two imaging systems occurs due to the object surface roughness. For instance, ultrasonic speckle is an interference effect caused by the scattering of the ultrasonic beam from microscopic tissue inhomogeneities [6]. The resulting granular pattern does not fully represent the actual tissue microstructure. In SAR imagery, speckle noise arises from random variations in earth surface roughness.

Speckle noise is considered as signal dependent and spatially correlated. The correlation of speckle can be observed from the coarseness, texture, or the speckle size of a speckle image [4]. An interesting property of speckle is that the ensemble mean of the speckle image is equal to the incoherent image of the original object [4]. This property serves as the basis for the frame averaging technique which is used as a speckle reduction method. In frame averaging, multiple frames of uncorrelated speckle images of the same object are generated and averaged on an intensity basis. This averaging process increases the signal to noise ratio from one to $M^{1/2}$ where M is the number of uncorrelated speckle images used. Even though frame averaging reduces speckle noise considerably, it possesses the drawback of requiring multiple frames of the original speckle image and thus, demands more acquisition and computation time.

2.2 The Speckle Noise Model

Over the years, the interest in applying image enhancement and restoration techniques to speckle reduction has increased. Most of these techniques, however, have assumed that speckle noise is multiplicative and have used multiplicative noise filtering algorithms to restore images corrupted with speckle. If speckle is regarded as multiplicative noise, then the correlation property, which is an important property for speckle reduction, is completely ignored. Thus, the multiplicative noise model can be considered only as a rough approximation of speckle noise representation [17].

The noise model that was used in this work is based on the model formulated by Kuan et al. [4]. They have modeled the speckle based on the physical process of coherent image formation. Thus, this model takes signal dependent effects of speckle into consideration and represents the higher order statistical properties that are important to the restoration procedure.

Kuan et al. considered signals with smaller bandwidths than the noise spectrum in the derivation of their speckle noise model. In this situation, the speckle intensity image is undersampled so that the sampling interval is greater than the correlation length of the speckle. This allows the correlation information of the speckle to be considered negligible and then to treat speckle samples as if they are independent of each other.

For the case of independent speckle samples, the speckle intensity g(k,l) can be represented as a multiplicative noise model such as,

$$g(k,l) = n(k,l)\, I(k,l), \tag{2.1}$$

where I(k,l) is the incoherent image of the original object through the same imaging system. n(k,l) is a signal dependent, white noise process with a normalized negative exponential probability distribution function (PDF), unit mean, and unit variance. The PDF is thus given by,

$$p[n(k,l)] = \begin{cases} \exp[-n(k,l)], n(k,l) \geq 0 \\ 0, \text{otherwise.} \end{cases} \tag{2.2}$$

This model essentially describes the speckle noise of an image in a multiplicative form, however including a limitation placed on its applications. Note that the multiplicative noise model for speckle could only be used in situations where the degraded image has been sampled coarsely enough so that the degradation at any point can be assumed to be independent of that at all other points [17].

As discussed in section 2.1, in certain applications, several independent speckle frames of the same object are available and a frame averaging technique can be employed to increase the signal-to-noise ratio. The average of M independent speckle images is

$$g_a(k,l) = \frac{1}{M}\sum_{i=1}^{M} g_i(k,l), \tag{2.3}$$

where $g_i(k,l)$ is the i^{th} image frame. $g_a(k,l)$, the average of M frames is shown to be the maximum likelihood estimate of the undegraded image [4].

CHAPTER 3

LINEAR FILTERS

Since the early development of signal and image processing, linear filters have been used as the primary restoration tools [3]. Today, image restoration based on the use of a wavelet transform has drawn the attention of many researchers [14], and has proven to be a versatile tool. The ability of wavelet transforms to decompose images into multiple resolutions aids the analysis of noisy images and removal of noise.

This chapter gives a brief description of the wavelet theory which was used in the implementation of the wavelet transform domain linear filter in our work. Section 3.1.1 discusses the derivations of the continuous time wavelet transform and series. Section 3.1.2 introduces the multiresolution representation of functions using wavelets which serves as the backbone of our noise suppressing linear filter. The discrete time wavelet series and the discrete wavelet transform are derived in sections 3.1.3 and 3.1.4, respectively. Section 3.2.1 discusses the multiresolution decomposition of images. Finally, section 3.2.2 explains the wavelet filtering algorithm.

3.1 Wavelet Theory

3.1.1 The Continuous-Time Wavelet Transform and Series

The best way to understand the mathematical derivations of the wavelet transform is by first analyzing the familiar Fourier transform. The continuous-time Fourier transform (CTFT=$F(\omega)$) is defined as the inner product of the signal $f(x)$ with the basis function,

$e^{-j\omega x}$. Mathematically, CTFT is written as,

$$F(\omega) = \int_{-\infty}^{\infty} f(x) e^{-j\omega x} dx, \tag{3.1}$$

where x is the time (location) variable and ω is the frequency variable. $F(\omega)$ in (3.1) denotes the Fourier coefficients. Any signal f(x) can then be written in terms of the appropriate Fourier coefficient as,

$$f(x) = \frac{1}{2\pi} \int_{-\infty}^{\infty} F(\omega) e^{j\omega x} d\omega. \tag{3.2}$$

The CTFT possesses several disadvantages when applied in practice. As shown in (3.1), all time information of the signal is required to obtain the Fourier transform at a single frequency. In other words, past and future information is needed to accurately reconstruct a signal. Also, all signals are not stationary in reality. If a sharp discontinuity is present in a signal, its Fourier representation will contain many sine and cosine terms that are attributed to the discontinuity. Therefore, the transformation of a non-stationary signal results in many Fourier coefficients which spread out over the entire frequency axis.

In order to overcome its drawbacks, the CTFT was slightly modified yielding the short-time Fourier transform, (STFT). The STFT positions a window function w(x) at b on the time (location) axis, and calculates the Fourier transform of the windowed signal as,

$$F(\omega, b) = \int_{-\infty}^{\infty} f(x) w(x - b) e^{-j\omega x} dx. \tag{3.3}$$

This transformation is time (location) dependent, and thus provides a time-frequency description of the signal. The drawback of the STFT however, is the fixed window size. In signal analysis, a narrow time-window for distinguishing high frequency phenomena and a wide time-window for analyzing low frequency behavior are preferred. Thus, the STFT is obviously not suitable for analyzing signals with both very high and very low frequencies.

The continuous-time wavelet transform (CTWT) mitigates the time-frequency resolution limitations of the STFT [18]. It uses a basis function with scaling (dilating) and shifting parameters a and b, respectively. Therefore, the CTWT basis function is defined as,

$$\psi_{a,b}(x) = \frac{1}{\sqrt{a}}\psi\left(\frac{x-b}{a}\right), \qquad a, b \in R, \tag{3.4}$$

where R denotes the set of real numbers. The transform kernel or the prototype function $\psi(x)$ is called the mother wavelet [18]. It is a zero-mean bandpass function. The wavelet transform of a given signal f(x) is defined as,

$$W(a,b) = \int_{-\infty}^{\infty} \psi_{a,b}(x) f(x) dx. \tag{3.5}$$

$\psi_{a,b}(x)$, the basis functions, are real and oscillatory. They will either fade away as time approaches plus or minus infinity, or be zero outside a support interval. The basis functions are also called wavelets and can be considered as dilated and shifted versions of the prototype function $\psi(x)$. For large values of a, the basis function becomes dilated version of the prototype wavelet, and for small a, it becomes a contracted version of the wavelet function, and it corresponds to lower and higher frequency bands, respectively in the frequency domain. Thus, the scaling parameter provides a flexibility in the time-frequency resolution of the signal. The ability to adapt to characteristics of a signal is a desired feature in signal decomposition, and hence, the CTWT offers an efficient representation of signals.

In order to enable the reconstruction of f(x) from its CTWT, the prototype function $\psi(x)$ should satisfy the following condition,

$$C_\psi = \int_0^\infty \frac{|\psi(\omega)|^2}{\omega} d\omega < \infty. \tag{3.6}$$

Here, $\psi(\omega)$ denotes the Fourier transform of $\psi(x)$, and C_ψ is a constant. Since $\psi(x)$ shows a decay at infinity, (3.6) implies that the function $\psi(x)$ has a zero-mean, i.e.,

$$\int_{-\infty}^{\infty} \psi(x) dx = 0. \tag{3.7}$$

Thus, a signal f(x) can be expressed as,

$$f(x) = \frac{1}{C_\psi} \int_{-\infty}^{\infty} \int_0^{\infty} W(a,b) \psi_{a,b}(x) \frac{da db}{a^2}. \tag{3.8}$$

The wavelet transform is defined as continuous if the scaling and translation parameters a and b, respectively are continuous. The two inherent drawbacks of the CTWT are redundancy and impracticality [18]. However, these problems can be solved by discretizing the transform parameters a and b. For discretization, the transform parameters a and b can be defined as follows:

$$a = a_0^m, \quad b = nb_0a_0^m, \quad m,n \in Z, \quad a_0 > 1, \quad b_0 > 0. \tag{3.9}$$

Z denotes the set of integers. Then, the corresponding basis functions for the discretized a and b are,

$$\psi_{m,n}(x) = a_0^{-m/2}\psi\left(a_0^{-m}x - nb_0\right). \tag{3.10}$$

We can now express any signal $f(x) \in L^2(R)$ as,

$$f(x) = \sum_m \sum_n d_{m,n}\psi_{m,n}(x). \tag{3.11}$$

For $a_0=2$, $b_0=1$, there exists a very unique choice of ψ such that the $\psi_{m,n}$ constitute an orthonormal basis, so that,

$$d_{m,n} = \int_{-\infty}^{\infty} f(x)\psi_{m,n}dx, \tag{3.12}$$

where $d_{m,n}$ is called the continuous-time wavelet series (CTWS).

3.1.2 Multiresolution Analysis

Multiresolution analysis, a mathematical representation developed by Mallat for the wavelets [19], provides a framework for an understanding of wavelet bases. It is a method of simultaneously observing a signal at successive scales. Further, it enables the use of wavelet bases in image analysis in a very efficient manner, and generates fast computation algorithms.

Let $L^2(R)$ denote the vector space of measurable, square-integrable one-dimensional functions f(x). In multiresolution analysis, $L^2(R)$ can be considered as a hierarchy of embedded subspaces V_m such that,

$$\ldots \subset V_2 \subset V_1 \subset V_0 \subset V_{-1} \subset V_{-2} \ldots,$$

$$\bigcap_{m \in Z} V_m = \varnothing, \qquad \overline{\bigcup_{m \in Z} V_m} = L^2(R). \tag{3.13}$$

These V_m also have the property such that for each function $f(x) \in V_m$, a contracted version of it is contained in the subspace V_{m-1}, i.e.,

$$f(x) \in V_m \quad \Leftrightarrow \quad f(2^m x) \in V_{m-1}. \tag{3.14}$$

In a multiresolution analysis, there is a function $\phi_m(x) \in V_m$, such that its dilated and translated versions,

$$\phi_{m,n}(x) = 2^{-\frac{m}{2}} \phi(2^{-m}x - n) \tag{3.15}$$

constitute an orthonormal basis for V_m. These basis functions are called scaling functions since they construct the scaled versions of functions in $L^2(R)$.

Now, W_m are defined as the orthogonal complements of the spaces V_m with respect to V_{m-1}, such that,

$$V_{m-1} = V_m \oplus W_m, \qquad V_m \perp W_m,$$

$$\bigcap_{m \in Z} W_m = \varnothing, \qquad \overline{\bigcup_{m \in Z} W_m} = L^2(R). \tag{3.16}$$

Here, we consider a function $\psi(x)$, which is the same prototype or mother wavelet function as in section 3.1.1. The dilated and translated versions of $\psi(x)$,

$$\psi_{m,n}(x) = 2^{-m/2} \psi(2^{-m}x - n) \tag{3.17}$$

form an orthonormal basis for $L^2(R)$. These functions $\psi_{m,n}(x)$ are the same as the wavelet functions found in (3.10) with $a_0=2$ and $b_0=1$.

Through multiresolution analysis, a function $f(x)$ in $L^2(R)$ can be viewed as a succession of approximations by functions $f_m(x)$ in V_m. That is,

$$f(x) = \lim_{m \to \infty} f_m(x). \tag{3.18}$$

This gives the feasibility to observe the function at different resolutions or scales. If m, the scaling parameter or level is high, then the function in V_m is a coarse approximation of f(x) where details are neglected. On the contrary, if m is low, a detailed approximation of f(x) results.

$f_m(x)$ is viewed as an orthogonal projection of f(x) onto V_m. Therefore,

$$f_m(x) = \sum_n \langle \phi_{m,n}(x), f(x) \rangle \phi_{m,n}(x) = \sum_n c_{m,n} \phi_{m,n}(x). \tag{3.19}$$

The wavelet functions $\psi_{m,n}$ enable us to write any function f(x) in $L^2(R)$ as a sum of projections on W_j, $j \in R$ as,

$$f(x) = \sum_{j=-\infty}^{\infty} e_j(x), \tag{3.20}$$

where,
$$e_j(x) = \sum_n \langle \psi_{j,n}(x), f(x) \rangle \psi_{j,n}(x) = \sum_n d_{j,n} \psi_{j,n}(x). \tag{3.21}$$

At a selected level m, the signal f(x) can then be written as a sum of a low resolution part $f_m(x) \in V_m$ and a number of detail parts $e_j(x) \in W_j$, such as,

$$\begin{aligned} f(x) &= f_m(x) + \sum_{j=-\infty}^{\infty} e_j(x) \\ &= \sum_n \langle \phi_{m,n}(x), f(x) \rangle \phi_{m,n}(x) + \sum_{j=-\infty}^{m} \sum_n \langle \psi_{j,n}(x), f(x) \rangle \psi_{j,n}(x) \\ &= \sum_n c_{m,n} \phi_{m,n}(x) + \sum_{j=-\infty}^{m} \sum_n d_{j,n} \psi_{j,n}(x). \end{aligned} \tag{3.22}$$

Therefore, in multiresolution analysis we deal with two functions; the mother wavelet ψ and a scaling function ϕ. For more detail on multiresolution wavelet transforms, see Mallat [19] and Daubechies [20].

3.1.3 The Discrete-Time Wavelet Series

For our filtering algorithm, the signal we wish to transform is an image. Thus, it is not a continuous, but a discrete signal. In this section we derive the formulae for the discrete time wavelet series (DTWS) using the fundamentals of multiresolution analysis discussed in Section 3.1.2.

Every discrete signal c_n can be considered as a sequence of weights of a set of scaling functions $\phi_{0,n}(x)$ representing a continuous function $f_0(x) \in V_0$. Therefore, $f_0(x)$ can be written as,

$$f_0(x) = \sum_n c_{0,n}\phi_{0,n}(x). \tag{3.23}$$

By incorporating the idea of multiresolution, $f_0(x)$ can be decomposed into two functions, $f_1(x) \in V_1$ and $e_1(x) \in W_1$ that contain the overall characteristics and the details of $f_0(x)$, respectively:

$$f_0(x) = f_1(x) + e_1(x) = \sum_k c_{1,k}\phi_{1,k}(x) + \sum_k d_{1,k}\psi_{1,k}(x). \tag{3.24}$$

This process can be continued on $f_1(x)$ and then until the desired decomposition is obtained.

It can be further shown that the coefficients $c_{j,k}$ and $d_{j,k}$ are calculated iteratively without the explicit use of the functions $\phi(x)$ and $\psi x)$ by,

$$c_{j,k} = 2^{½}\sum_n h_{2k-n}c_{j-1,n}, \tag{3.25}$$

$$d_{j,k} = 2^{½}\sum_n g_{2k-n}c_{j-1,n}. \tag{3.26}$$

Note that $c_{j,k}$ and $d_{j,k}$ have just half the length of $c_{j-1,k}$, and h_n and g_n are defined as follows:

$$h_n = 2^{\frac{1}{2}} \int \phi(x-n)\phi(2x)dx \text{, and} \tag{3.27}$$

$$g_n = (-1)^{1-n} h(1-n), \tag{3.28}$$

where h is a lowpass filter and g is a highpass filter [19]. The following restrictions are made on the filters h_n and g_n.

$$2\sum_{k}\left(h_{n+2k}h_{p+2k} + g_{n+2k}g_{p+2k}\right) = \delta_{n,p}, \tag{3.29}$$

$$2\sum_{k} h_{n+2k}h_{n+2p} = 2\sum_{n} g_{n+2k}g_{n+2p} = \delta_{k,p}, \tag{3.30}$$

$$2\sum_{n} h_{n+2k}g_{n+2p} = 0. \tag{3.31}$$

3.1.4 The Discrete Wavelet Transform

The discrete wavelet transform (DWT) is an efficient technique that is used to transform a discrete signal of finite length to a new signal of equal length. It can be represented as a matrix operator. The elements of the matrix depend on the basis function used. For simplicity, here we have chosen Daubechies' four coefficients in deriving formulae for the DWT.

Daubechies derived an algorithm to generate wavelet coefficients based on two properties. The first property takes the orthogonality condition placed on the wavelet filters into consideration. If the wavelet filter was taken to be W, then $WW^{-1}=1$, where W^{-1} is the inverse of the filter W. According to the second property, filter g should have a zero response to a smooth part of a signal since g is a highpass filter. To obtain a zero response, g must have a certain number of vanishing moments. Therefore, the wavelet filter W can be represented by,

$$W = \begin{bmatrix} h_0 & h_1 & h_2 & h_3 & & & & & & & \\ g_0 & g_1 & g_2 & g_3 & & & & & & & \\ & & h_0 & h_1 & h_2 & h_3 & & & & & \\ & & g_0 & g_1 & g_2 & g_3 & & & & & \\ & & & & & & \cdots\cdots & & & & \\ & & & & & & \cdots\cdots & & & & \\ & & & & & & & h_0 & h_1 & h_2 & h_3 \\ & & & & & & & g_0 & g_1 & g_2 & g_3 \\ h_2 & h_3 & & & & & & & & h_0 & h_1 \\ g_2 & g_3 & & & & & & & & g_0 & g_1 \end{bmatrix}. \tag{3.32}$$

The blank elements of the matrix W represent zeros. By using (3.28), the filters g can be found in terms of h. If we consider a signal of length eight, we can write the forward DWT and the inverse DWT, respectively, as follows:

$$\begin{bmatrix} c_{1,0} \\ c_{1,1} \\ c_{1,2} \\ c_{1,3} \\ d_{1,0} \\ d_{1,1} \\ d_{1,2} \\ d_{1,3} \end{bmatrix} = \sqrt{2} \begin{bmatrix} h_0 & h_1 & h_2 & h_3 & & & & \\ & & h_0 & h_1 & h_2 & h_3 & & \\ & & & & h_0 & h_1 & h_2 & h_3 \\ h_2 & h_3 & & & & & h_0 & h_1 \\ h_3 & -h_2 & h_1 & -h_0 & & & & \\ & & h_3 & -h_2 & h_1 & -h_0 & & \\ & & & & h_3 & -h_2 & h_1 & -h_0 \\ h_1 & -h_0 & & & & & h_3 & -h_2 \end{bmatrix} \begin{bmatrix} c_{0,0} \\ c_{0,1} \\ c_{0,2} \\ c_{0,3} \\ c_{0,4} \\ c_{0,5} \\ c_{0.6} \\ c_{0,7} \end{bmatrix}, \tag{3.33}$$

$$\begin{bmatrix} c_{0,0} \\ c_{0,1} \\ c_{0,2} \\ c_{0,3} \\ c_{0,4} \\ c_{0,5} \\ c_{0,6} \\ c_{0,7} \end{bmatrix} = \sqrt{2} \begin{bmatrix} h_0 & & & h_2 & h_3 & & & h_1 \\ h_1 & & & h_3 & -h_2 & & & -h_0 \\ h_2 & h_0 & & & h_1 & h_3 & & \\ h_3 & h_1 & & & -h_0 & -h_2 & & \\ & h_2 & h_0 & & & h_1 & h_3 & \\ & h_3 & h_1 & & & -h_0 & -h_2 & \\ & & h_2 & h_0 & & & h_1 & h_3 \\ & & h_3 & h_1 & & & -h_0 & -h_2 \end{bmatrix} \begin{bmatrix} c_{1,0} \\ c_{1,1} \\ c_{1,2} \\ c_{1,3} \\ d_{1,0} \\ d_{1,1} \\ d_{1,2} \\ d_{1,3} \end{bmatrix}. \tag{3.34}$$

By using the orthogonality conditions described in (3.29) through (3.31), the filters h can be found as,

$$h_0 = \frac{1+\sqrt{3}}{4\sqrt{2}}, \tag{3.35}$$

$$h_1 = \frac{3+\sqrt{3}}{4\sqrt{2}}, \tag{3.36}$$

$$h_2 = \frac{3-\sqrt{3}}{4\sqrt{2}}, \text{and} \tag{3.37}$$

$$h_3 = \frac{1-\sqrt{3}}{4\sqrt{2}}. \tag{3.38}$$

The multiresolution analysis of the wavelet transform represents the original signal by consecutively decomposing it into lower resolutions, while keeping all the detail information between each consecutive resolution. If the original signal is of length N, after the transformation, it is decomposed into smooth and detailed vectors, each of length N/2. Then, the N/2 smooth vector is further decomposed to result in an N/4 smooth vector and an N/4 detailed vector. This process can be continued until the length of the smooth vector becomes one. Figure 3.1 shows a block diagram of this wavelet transform process.

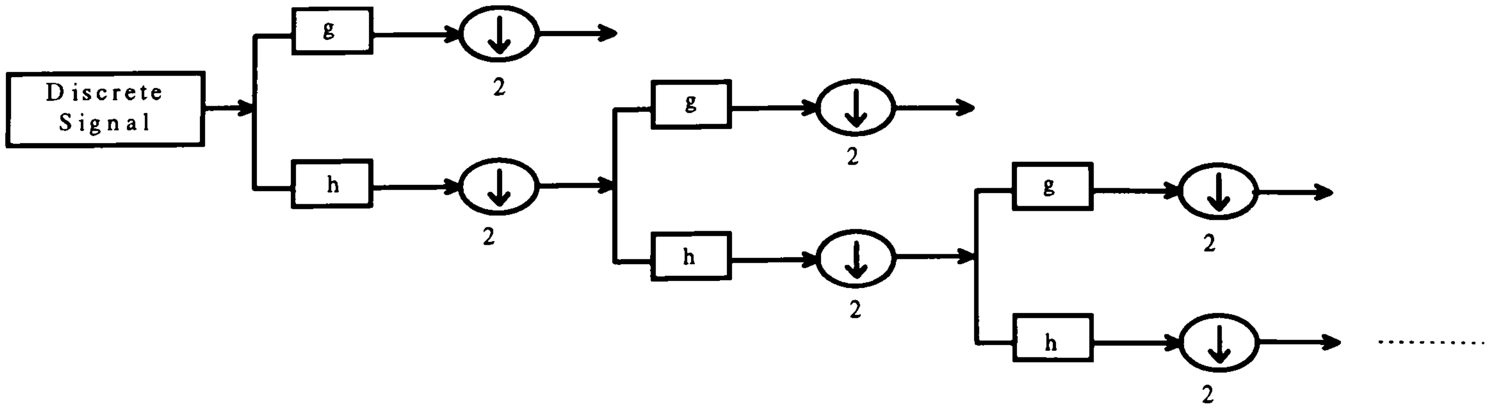

Figure 3.1. Implementation of the 1-D wavelet transform.

3.2 Wavelet Transform Domain Filtering Algorithm

3.2.1 Multiresolution or Pyramidal Decomposition of Images

With a separable approximation, multiresolution wavelet filters could easily be extended to the two dimensional case, i.e., in analysis of images [19]. In the two-dimensional multiresolution wavelet transform, we must define a scaling function $\phi(x,y)$ and a wavelet function $\psi(x,y)$ that are separable. That is,

$$\phi(x,y) = \phi(x)\phi(y) \tag{3.39}$$

and

$$\psi(x,y) = \psi(x)\psi(y). \tag{3.40}$$

Also, the combinations of scaling and wavelet functions can be defined as,

$$\phi(x,y)_l = \phi(x)\phi(y) \tag{3.41}$$

$$\psi(x,y)_h = \phi(x)\psi(y) \tag{3.42}$$

$$\psi(x,y)_v = \psi(x)\phi(y) \tag{3.43}$$

$$\psi(x,y)_d = \psi(x)\psi(y). \tag{3.44}$$

The computation of the 2-D DWT of an image is twofold. First, the 1-D wavelet transform (WT) is taken along each row of the image pixels by multiplying with the appropriate low and highpass filters h and g. Then, the lowpass and detail image parts are down sampled by two. The second part is taking the WT along each column of the reordered lowpass and detail image pixels by again multiplying with the appropriate h and g. The columns are again down sampled by two. The result of this operation is a decomposition of the image consisting of a lowpass L image in quadrant one, a vertical error image D_v in quadrant two, a horizontal error image D_h in quadrant three, and a diagonal error image D_d in quadrant four. Continuous decomposition of the lowpass image will yield multiresolution WT decomposition of the image. Figures 3.2 and 3.3 show first level and second level WT decompositions of an image, respectively. Figure 3.4 shows a two-level wavelet decomposition of the standard "Lena" image using Daubechies' 4 coefficients.

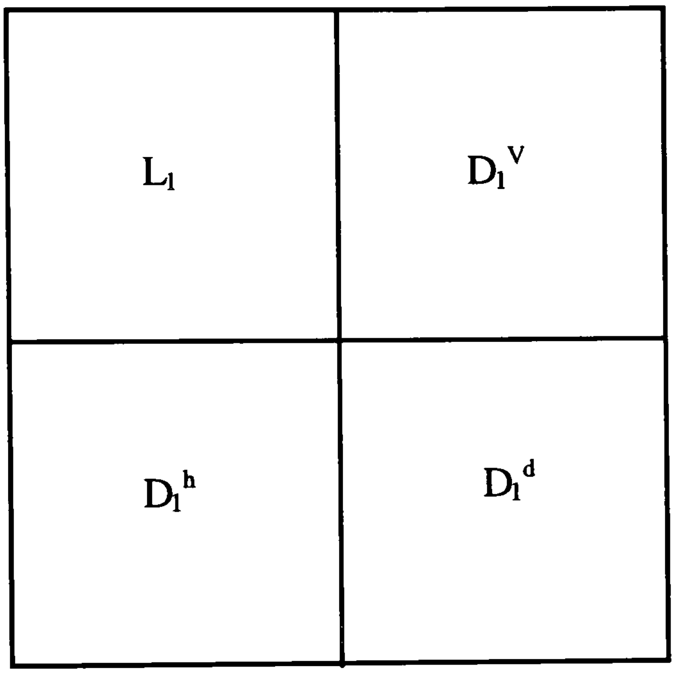

Figure 3.2. First level wavelet decomposition of an image.

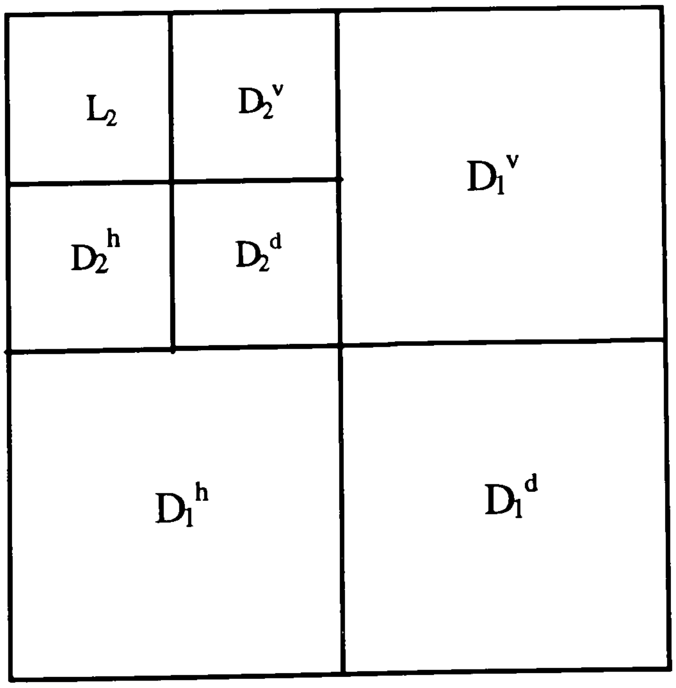

Figure 3.3. Second level wavelet decomposition of an image.

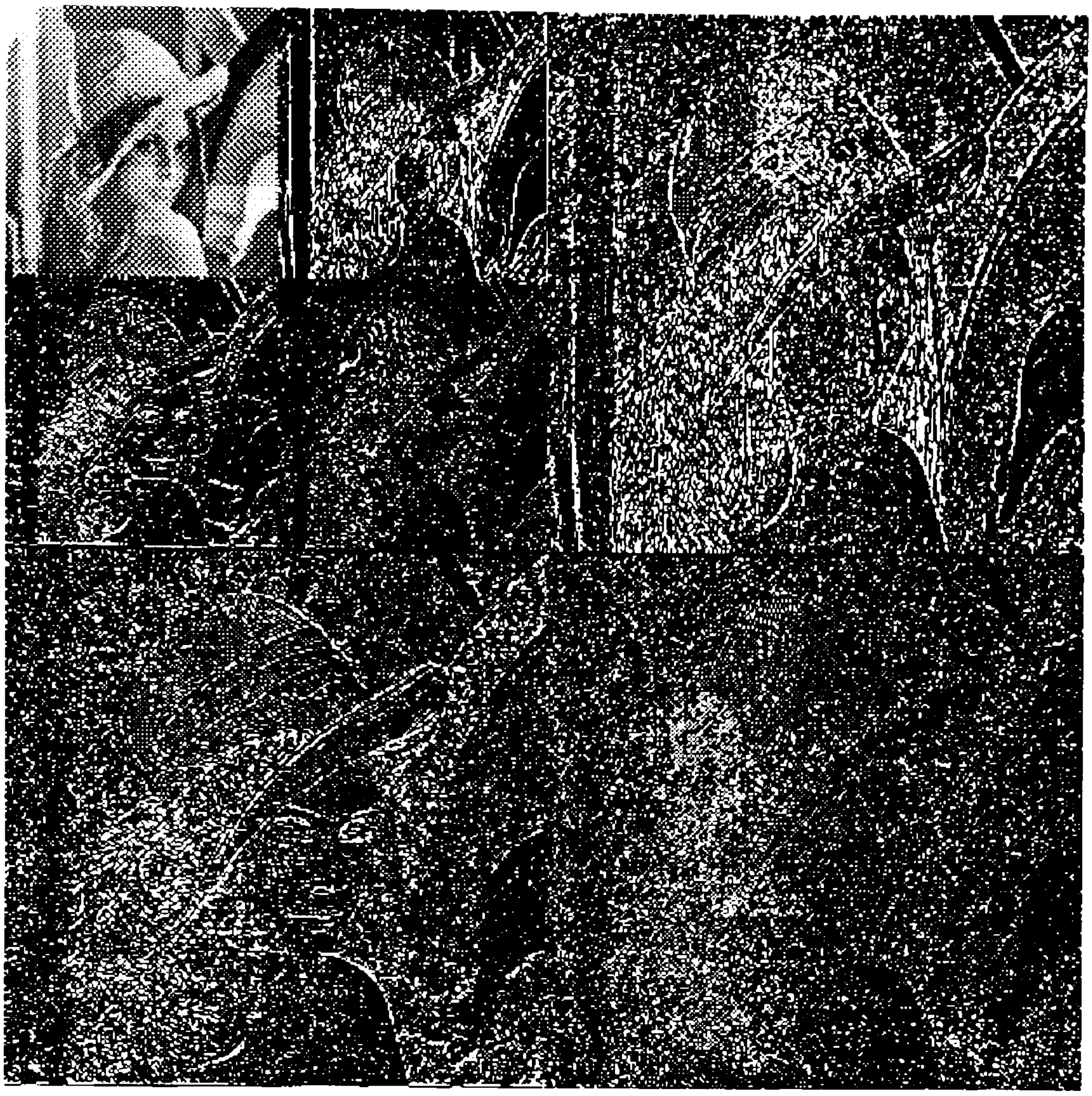

Figure 3.4. Second level wavelet decomposition of 512x512, 8 bits/pixel standard "Lena" image using Daubechies' 4 coefficients.

3.2.2 The Filtering Process

The concept of filtering a signal in the time-frequency domain has been employed for many years [5]. The wavelet domain filtering technique falls under this category of filtering. The ability of WTs to decompose images into multiple scales, as previously described in this chapter, facilitates the efficiency of noise suppression.

In our work, we perform a simple version of multiscale filtering. This is done by setting the wavelet coefficients of the image to zero in regions of the wavelet domain where the signal energy is observed to be smaller than the noise energy. Speckle noise energy is confined to small scales. Since fine-scale WT components represent localized high frequency features of the image, we can window these to zero and cancel some of the noise energy without degrading the image. This is similar in concept to lowpass filtering, in which the Fourier transform of the signal is windowed to zero at frequencies where the signal energy is much smaller than the noise energy. This selective discarding of noise components can be carried out at different decomposition levels of the image. An advantage of using the WT is that multiresolution filtering can be performed on a localized basis, smoothing some areas while leaving others unaffected.

CHAPTER 4

NONLINEAR FILTERS

Although the exact characteristics of the human visual system are not yet well understood, experimental results indicate that the first processing stages of the human visual system possess nonlinear characteristics [3]. Since this discovery, nonlinear filtering in image processing applications has seen a dynamic development. Nonlinear filters are proven to perform efficiently in restoring images degraded with noise. The two main nonlinear filtering techniques we have investigated in our research for speckle removal are conventional median filtering and morphological filtering using new connectivity preserving operators in an alternating sequential manner.

This chapter consists of the mathematical fundamentals used in deriving the algorithms of the two filtering techniques. Section 4.1 describes the mathematical morphology and the filtering algorithm. Sections 4.1.1 and 4.1.2 explain the fundamental operations of binary and gray level mathematical morphology for images, respectively. The need for new connectivity preserving morphological filters is discussed in section 4.1.3. Bounded closing and bounded opening, the two operations used in the connectivity preserving filters are introduced in section 4.1.4. Section 4.1.5 discusses the alternating sequential filtering based on bounded closing and bounded opening operations. Fast implementation of dilation and erosion is introduced in section 4.1.6. Finally, section 4.2 briefly discusses the median filtering technique.

4.1 Mathematical Morphology

Mathematical morphology is a powerful tool developed initially by Georges Matheron and Jean Serra [21] for geometrical shape analysis and description within an image. It uses a set theoretic approach to image analysis. The basic principle behind mathematical morphology is to probe the image with a "structuring element" and to evaluate the manner in which the structuring element fits or does not fit within the image. The structuring element is a small set of points or pixels. The information obtained after probing or analyzing an image by a structuring element depends on the choice of the structuring element itself.

4.1.1 Morphological Operations for Binary Images

Let a binary image, A, be represented as a subset of a two-dimensional Euclidean grid Z^2. B represents a small set called a structuring element which operates on set A. Here, brief descriptions of the basic morphological transformations are presented.

The erosion of a binary set A by another set B is defined as,

$$A \ominus B = \cap\,(x: B_x \subset A), \tag{4.1}$$

where B_x denotes the translation of the set B by x. In words, erosion is the set of all points x for which the translation of B by x fits inside of A. Erosion by a structuring element which contains its origin will result in a shrinking of the input image. Thus, in this case, eroded image can be considered as a subset of the input image. If the origin does not lie inside the structuring element, then the eroded image may not necessarily be a subset of the input image. Erosion can also be thought of as translating the input image by negatives of the co-ordinate points of the structuring element and intersecting all the translates.

The dilation of a binary set A by another set B is defined as,

$$A \oplus B = \cup (B_x : x \subset A). \tag{4.2}$$

In words, dilation is the union of translations of the input image A by all points in the structuring element B. If the origin is contained in the structuring element, then the dilation results in an expansion of the original image.

Dilation is considered to fill in small intrusions of the image and expand the white portions of the binary image. On the contrary, erosion is expected to eliminate small extrusions of the image and shrink the white portions of the binary image. Erosion and dilation are the two primary operations in mathematical morphology. The combinations of these two give rise to two other secondary operations, namely opening and closing.

The opening of a binary set A by another set B is defined as an iteration of erosion and dilation by,

$$A^\circ B = (A \ominus B) \oplus B = \cup (B_x : B_x \subset A). \tag{4.3}$$

That is, opening is the union of all translations of the structuring element that fit inside the input image. The parts of the input image where the structuring element cannot fit are thus removed as a result of the opening operation. The opening operation is such that it only preserves the parts of the white region where the structuring element can fit. The remaining thin white portions are turned black or opened.

The white portion of the opened image is a subset of the white portion of the input image. Therefore, opening is considered to be "antiextensive." Also, the result of multiple operations of opening is the same as the result of a single operation of opening. Hence, opening is considered as "idempotent."

The closing of a binary set A by another set B is defined as an iteration of dilation followed by erosion. That is,

$$A \bullet B = (A \oplus B) \ominus B, \tag{4.4}$$

and is essentially equivalent to the complement of the opening operation. Closing can be used to fill in the thin regions missing from the input image. The result of closing is such that it only preserves the parts of the black region of the binary image where the structuring element can fit. The remaining thin black portions are turned white or closed.

The white portion of the input image is a subset of the white portion of the closed image. Therefore, closing is considered to be "extensive." Also, the result of multiple operations of closing is the same as the result of a single operation of closing. Hence, closing is also considered as "idempotent."

Figure 4.1 illustrates the four basic morphological operations for a binary image. Figure 4.1(a) shows a binary set A in Z^2 and Figure 4.1(b) shows the structuring element B. The erosion operation of set A with B is shown in Figure 4.1(c). It is clear that the erosion has shrunk the white portion of the image and thus proves the antiextensivity. The dilation operation of set A by B is depicted in Figure 4.1(d) where it is clear that the white portion is expanded by the operation. This demonstrates the extensivity property of dilation. As illustrated in Figure 4.1(e), opening can be used to remove thin white regions where the structuring element cannot fit. Finally, the closing operation can be used to remove thin black regions or fill the thin regions missing from the set as shown in Figure 4.1(f).

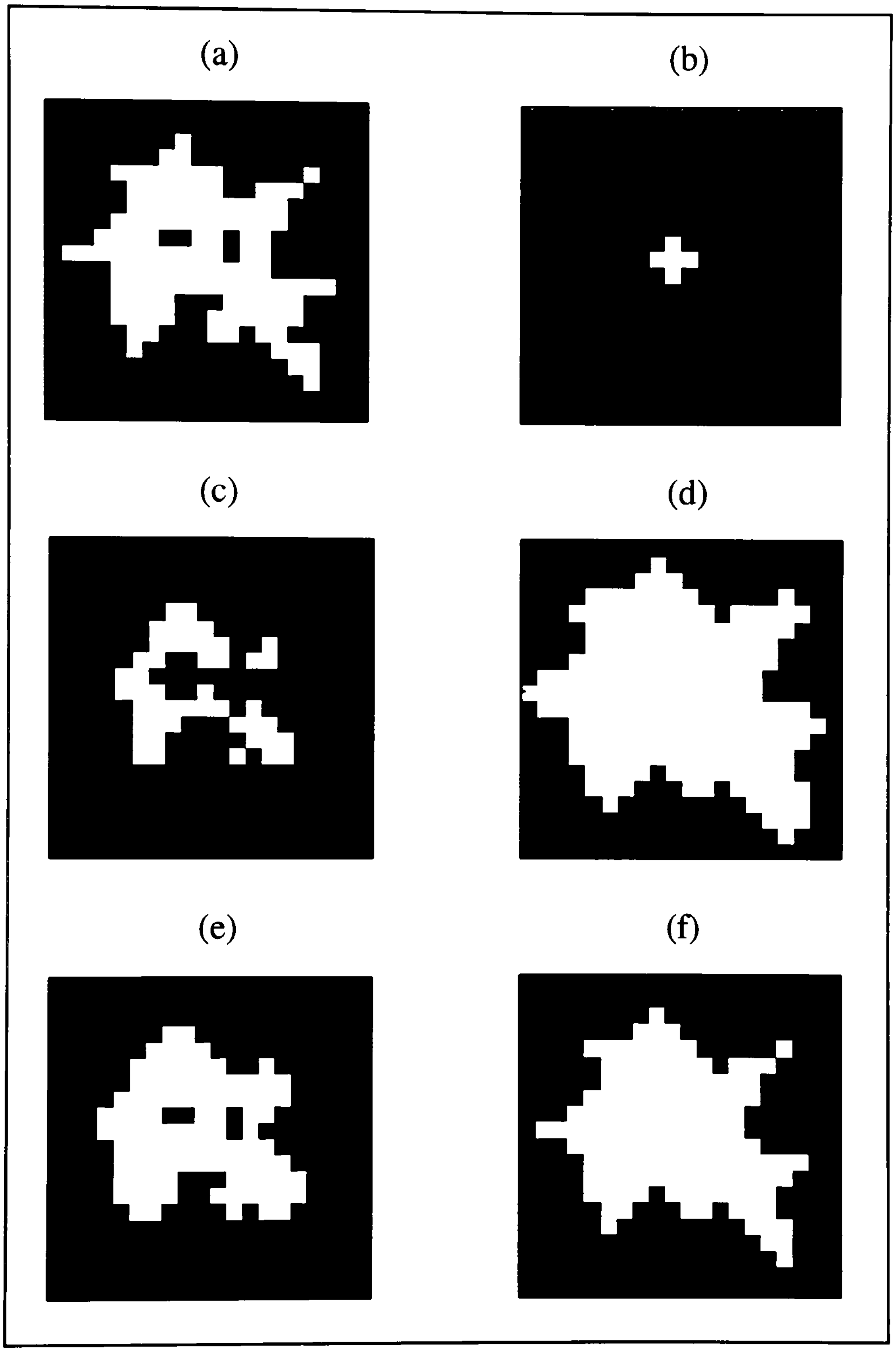

Figure 4.1. Basic morphological operations on a binary set in a 2D discrete space.
(a) Set A, (b) Structuring element B, (c) Erosion: $A \ominus B$,
(d) Dilation: $A \oplus B$, (e) Opening: $A^{\circ}B$, (f) Closing $A \bullet B$.

4.1.2 Morphological Operations for Gray Level Images

For the use of morphological operations, gray level images may be considered as fuzzy sets with image intensity values as membership values. Let $\mu_x(x)$ represent the membership function value of a point x in the fuzzy set X. Before defining gray-scale operations, we need to define the counterparts for the binary building blocks of union, intersection, and subset in terms of membership functions. They are as follows:

$$\text{Union:} \qquad R = P \cup Q \;\Rightarrow\; \mu_R(x) = \max(\, \mu_p(x)\,,\, \mu_Q(x)\,), \tag{4.5}$$

$$\text{Intersection:} \quad R = P \cap Q \;\Rightarrow\; \mu_R(x) = \min(\mu_p(x)\,,\, \mu_Q(x)), \tag{4.6}$$

and

$$\text{Subset:} R = P \subset Q \;\Rightarrow\; \mu_p(x) < \mu_Q(x). \tag{4.7}$$

Let A, the input image, be a fuzzy set with membership values $\mu_A(x)$. In our work, the structuring element B is still taken as a binary set. The morphological operations of gray level erosion and dilation for fuzzy sets are defined as follows:

$$\text{Erosion:} \qquad C = A \ominus B \;\Rightarrow\; \mu_C(x) = \min(\, \mu_A(y) : y \in (B_X)\,), \text{ and} \tag{4.8}$$

$$\text{Dilation:} \qquad D = A \oplus B \;\Rightarrow\; \mu_D(x) = \max(\, \mu_A(y) : y \in (B_X)\,). \tag{4.9}$$

By using definitions (4.5) through (4.9), most of the binary morphological operations can be extended to gray-scale or fuzzy morphology. For instance, the gray level opening and closing operations can be expressed as in (4.3) and (4.4), respectively, by incorporating the gray level erosion (4.8), and dilation (4.9) operations. The morphological operations stated in the rest of the chapter will be applicable to either binary or gray-scale images, unless otherwise mentioned. Some of the important properties of mathematical morphology are summarized next.

Properties of dilation and erosion:

(a) Antiextensivity of erosion and extensivity of dilation.

If o is the origin of the co-ordinate system and $o \in B$, $(A \ominus B) \subset A \subset (A \oplus B)$. (4.10)

(b) Associativity of dilation.

$$A \oplus (B \oplus C) = (A \oplus B) \oplus C \tag{4.11}$$

(c) $$A \ominus (B \oplus C) = (A \ominus B) \ominus C \tag{4.12}$$

(d) Behavior under a translation of the structuring element.

$$A \oplus (B_x) = (A \oplus B)_x \tag{4.13}$$

$$A \ominus (B_x) = (A \ominus B)_{-x} \tag{4.14}$$

Properties of opening and closing:

(a) Antiextensivity of opening and extensivity of closing.

$$(A^\circ B) \subset A \subset (A \bullet B) \tag{4.15}$$

(b) $$(D^\circ B) = D \Rightarrow (A^\circ D) \circ B = (A^\circ D) \text{ and } (A \bullet D) \bullet B = (A \bullet D) \tag{4.16}$$

(c) Idempotence of closing and opening.

$$(A \bullet B) \bullet B = (A \bullet B) \text{ and } (A^\circ B) \circ B = (A^\circ B) \tag{4.17}$$

(d) Behavior under a translation of the structuring element. Opening and closing are independent of the origin of the structuring element.

$$A^\circ (B_x) = A^\circ B \tag{4.18}$$

$$A \bullet (B_x) = A \bullet B \tag{4.19}$$

For more detail on mathematical morphology in image processing, see Dougherty [21].

4.1.3 The New Connectivity Preserving Filters

The standard gray-scale morphological opening and closing remove bright and dark regions of images, respectively where the structuring element cannot fit [15]. Thus, they possess the drawback of removing thin but long regions which could be useful information. A new connectivity preserving morphological filter has been proposed [15] to remove small spots (considered as noise) from thin but connected regions. It is proven that this filter retains the very fine image information while reducing noise significantly.

This filter uses two new operators called bounded opening and bounded closing to remove bright and dark regions (or spots), respectively which are constrained inside the boundary of a convex structuring element. The boundary of the convex structuring element as well as the convex structuring element itself are used in these operations. To reduce noise significantly, the structuring element size should be large compared to the noise spot size.

4.1.4 Bounded Closing and Bounded Opening

Two more operators are introduced here to build up the definitions of bounded closing and bounded opening. They are called "Boundary Erosion Region Dilation" (BERD) and "Boundary Dilation Region Erosion" (BDRE). The following discussion utilizes binary sets as images and structuring elements for simplicity. However, these operators are applicable to gray-scale image filtering as well [15].

Let A be an image and D a convex structuring element with the boundary B. Then, the boundary erosion region dilation (BERD) of A with (D,B) is defined as,

$$A \boxminus (D,B) = (A \ominus B) \oplus D. \tag{4.20}$$

Here, $\ominus$ and $\oplus$ are the usual erosion and dilation operators, respectively, and $\boxminus$ is the BERD operator.

The boundary dilation region erosion (BDRE) of A with (D,B) is defined as,

$$A \boxplus (D,B) = (A \oplus B) \ominus D. \tag{4.21}$$

$\ominus$ and $\oplus$ denote the usual erosion and dilation operators, respectively, and $\boxplus$ is the BDRE operator. By using the definitions of BERD and BDRE, the two filtering operators can be defined as follows.

Bounded Closing: $$A \odot (D,B) = \max(A, A \boxminus (D,B)) \tag{4.22}$$

Bounded Opening: $$A \circledcirc (D,B) = \min(A, A \boxplus (D,B)) \tag{4.23}$$

Some properties of the bounded closing operator, $\odot$, are:

(1) Bounded closing operation $A \odot (D,B)$, is extensive but not idempotent.

(2) If there exists a translate B_x of B such that a black region of A falls in the interior of B_x while B_x lies entirely in the white portion of A, then the operation $A \odot (D,B)$ turns the black region white.

(3) If a dark region of A does not lie in the interior of translate B_x of B while B_x lies in the white portion of A, then $A \odot (D,B) = A$.

Some properties of the bounded opening, $\circledcirc$ operator are:

(4) Bounded opening operation $A \circledcirc (D,B)$, is antiextensive but not idempotent.

(5) If there exists a translate B_x of B such that a white region of A falls in the interior of B_x while B_x lies entirely in the black portion of A, then the operation $A \circledcirc (D,B)$ turns the white region black.

(6) If a white region of A does not lie in the interior of translate B_x of B while B_x lies in the black portion of A, then A◎(D,B) = A.

The difference between the bounded closing operation and the usual closing operation is such that the former removes the dark region which can fit inside the interior of some translate of the structuring element while the latter removes the dark portion where the structuring element cannot fit. However, it is noteworthy that bounded closing may not remove a dark spot which can fit inside translates of some structuring element, but the boundary of the structuring element for any of these translates does not entirely lie in the white portion of the image. The role of bounded closing in removing dark spots is equivalent to the role of bounded opening in removing white spots in an image. More detail on these two new operators is found in Kher [15]. As mentioned before, the same concepts can be generalized to gray-scale morphology.

Figure 4.2 illustrates the BDRE operation of an image A (Figure 4.2(a)) with a convex structuring element D and its boundary B (Figure 4.2(b)). A is a set with a white spot and a long white element in a black background. Figure 4.2(c) shows the dilation operation. It is shown that when the image is dilated, some portion of the white spot is turned black. Hence, the original image is not a subset of the dilated image. This is due to the non-convex shape of the structuring element B. In the BDRE operation (Figure 4.2(d)), the white spot is removed, and the long element is preserved but with some changes. These changes in the long element are the same as when the original image is subjected to closing operation, as shown in Figure 4.2(f). Figure 4.2(e) illustrates the bounded opening operation. Here, the white spot is completely removed and the long element is preserved without any distortion.

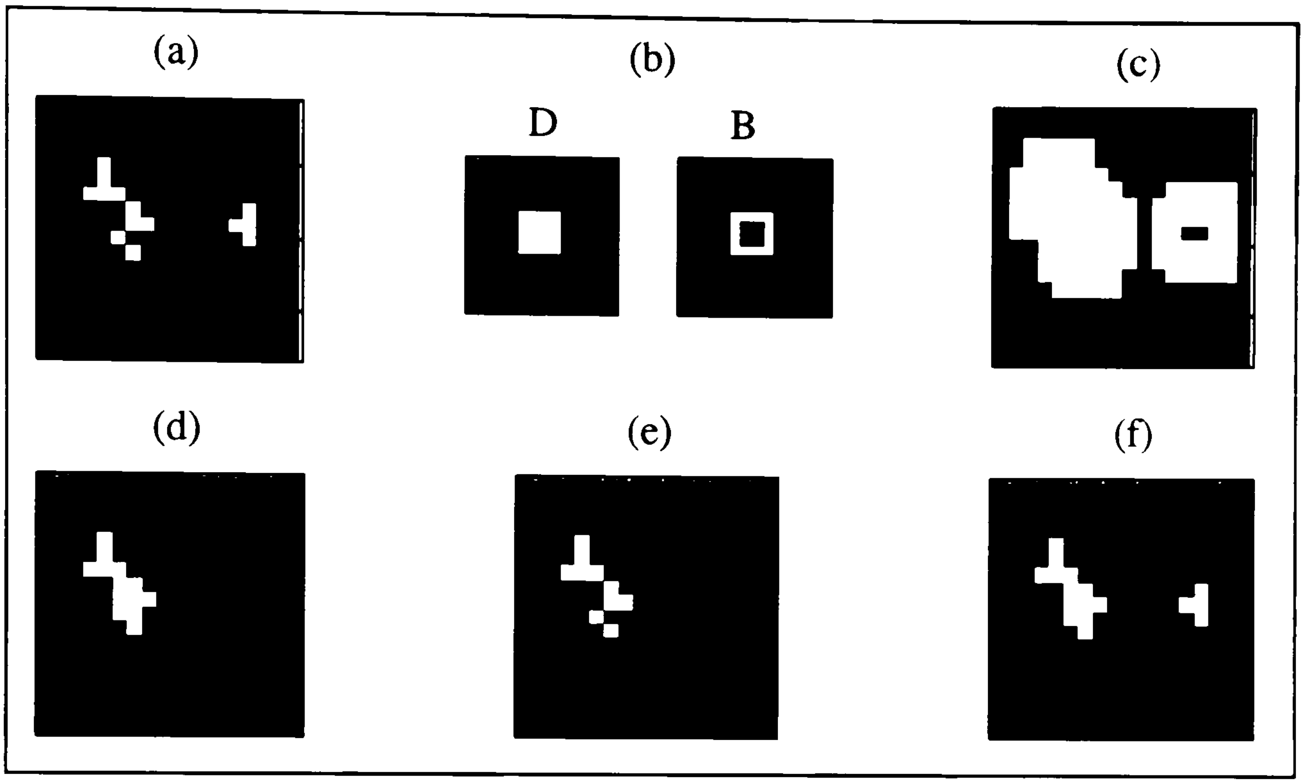

Figure 4.2. BDRE operation of an image. (a) Original binary image A.
(b) Structuring element D and its boundary B. (c) Dilation:$(A\oplus B)$.
(d) BDRE:$(A\oplus B)\ominus D$. (e) Bounded opening:$A\circledcirc(D,B)$. (f) Closing: $(A\bullet D)$.

4.1.5 Alternating Sequential Filtering Based on Bounded Closing and Bounded Opening

The simple opening and closing operations are used as filters to remove small noisy regions and, usually, a sequence of several opening and closing operations compose a filter. When a sequence of open-close or close-open filters are performed iteratively with successively larger structuring elements, it is called an alternating sequential filter (ASF). To probe an input image A with a structuring element B, the general form of a k^{th} order ASF is given by,

$$ASF(A \wedge B \vee B)^K = A \wedge B \vee B \wedge B^2 \vee B^2 \ldots\ldots \wedge B^K \vee B^K. \tag{4.24}$$

The operations $\wedge$ and $\vee$ are performed from left to right and are called algebraic closing and algebraic opening, respectively. An operation is called algebraic closing if it satisfies the conditions extensivity and idempotence and an operation is called algebraic opening if it satisfies the conditions antiextensivity and idempotence. Standard morphological closing and opening satisfy these conditions and hence they are considered as algebraic closing and algebraic opening operations, respectively. Consequently, they can be used as ASFs.

The idempotence property is not satisfied by either bounded closing or bounded opening operations. This fact is illustrated in Figure 4.3 for the case of bounded closing. The image in Figure 4.3(a) comprises a set of five noise spots and a connected region. Figure 4.3(b) shows the convex structuring element D and the boundary B used in the bounded closing operation. As shown in Figure 4.3(c), the boundary B of the structuring element D can lie around only three noise spots without overlapping with any other region of the set. Therefore, as shown in Figure 4.3(d), the first operation of bounded closing removes only these three spots. Once these three spots are removed, the boundary B is free to lie around the remaining two noise spots without hitting any other part of the set (Figure 4.3(e)). Then, as shown in Figure 4.3(f), a second operation of bounded closing operation removes the last two noise spots. Further operations of bounded closing will not change the set in Figure 4.3(f) anymore. Therefore, the bounded closing operation is not idempotent and likewise, it can be illustrated that neither is the bounded opening operation.

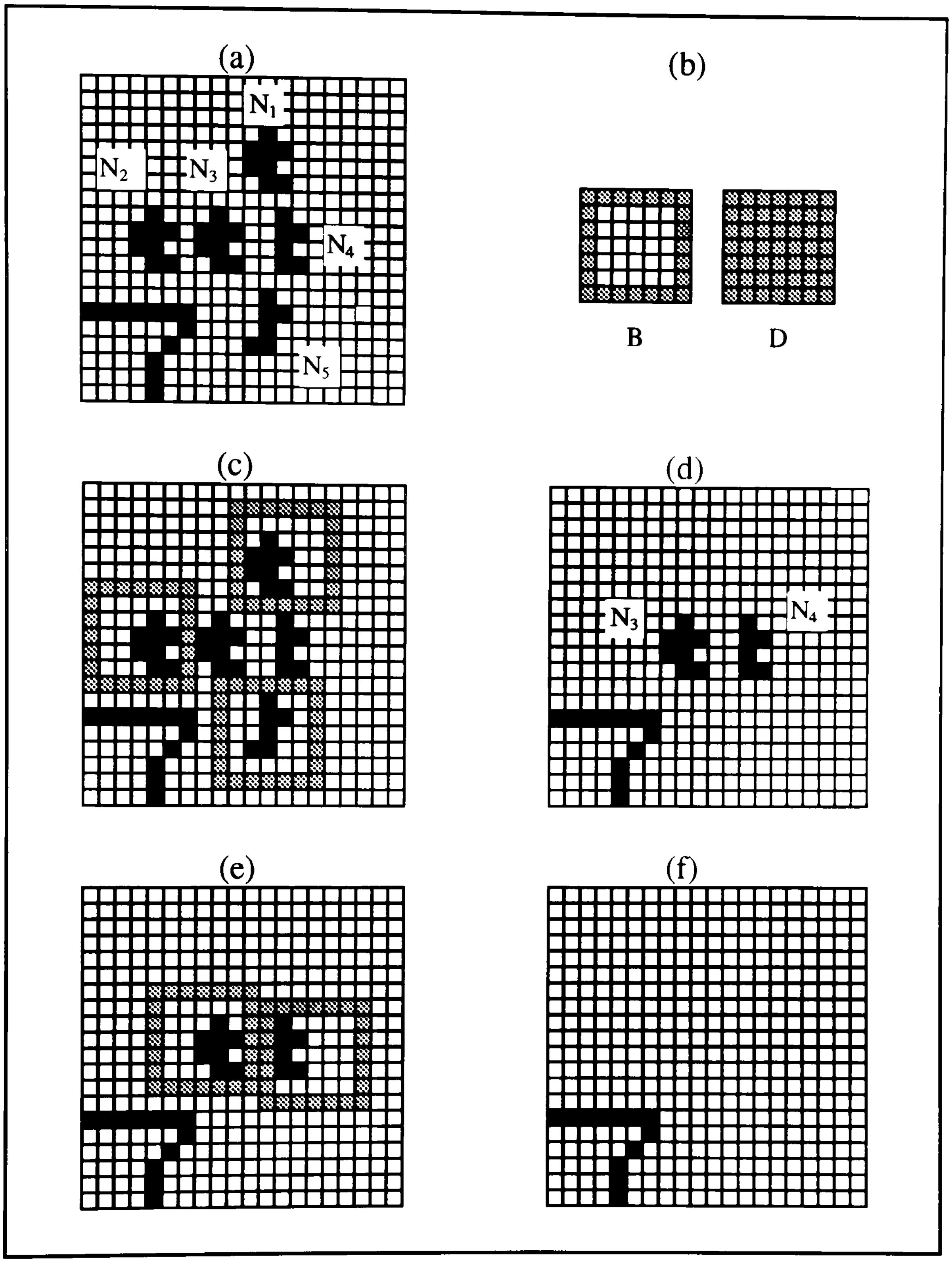

Figure 4.3. Lack of idempotence of bounded closing:
(a) Input image with noise spots N_1-N_5 and a thin connected region.
(b) Structuring element (D,B). (c) Possible positions of B around N_1,N_2, and N_5. (d) First operation of bounded closing. (e) Possible positions of B around N_3 and N_4. (f) Second operation of bounded closing.

However, a repeated applications of bounded closing result in a practically idempotent operation. The same argument is held true for bounded opening. Then, the bounded closing and bounded opening operations can be used to yield algebraic closing and algebraic opening operations, respectively as follows:

$$A\odot(D,B) = (A\odot(D,B))^{m} = A\odot(D,B)\odot(D,B)\text{..... m times.} \qquad (4.25)$$

$$A\circledcirc(D,B) = (A\circledcirc(D,B))^{m} = A\circledcirc(D,B)\circledcirc(D,B)\text{..... m times.} \qquad (4.26)$$

m is a small integer and practically takes a value between two to five [15].

Images consist of noise spots of different sizes. In such cases, structuring element pairs of different sizes are used to filter the noise effectively. It is proven statistically that the size of the structuring element should be larger than the noise spot [15]. Thus, a practical connectivity preserving k^th^-order ASF of the form (4.24) using different sizes of structuring elements can be defined by using the algebraic closing in (4.25) and algebraic opening in (4.26) as,

$$\mathrm{ASF}(A\odot(D,B)\circledcirc(D,B))^{K}$$

$$=A\odot(D,B)\circledcirc(D,B)\odot(D^{2},B^{2})\circledcirc(D^{2},B^{2}))....\odot(D^{i},B^{i})\circledcirc(D^{i},B^{i}))...... \qquad (4.27)$$

D^{i} is the structuring element of the i^th^ size and B^{i} is its boundary.

4.1.6 Fast Implementation of Dilation and Erosion

Erosions and dilations with large sizes of structuring elements can easily be obtained by using fast algorithms. Equations (4.11) and (4.12) imply that a dilation or an erosion with a large structuring element can be replaced by multiple dilations or erosions with smaller structuring elements. This is illustrated in Figure 4.4. A dilation/erosion with a structuring element R is equivalent to a dilation/erosion with P followed by a dilation/erosion with Q. The use of small structuring elements over the large ones in dilation and erosion operations results in the reduction of computational time.

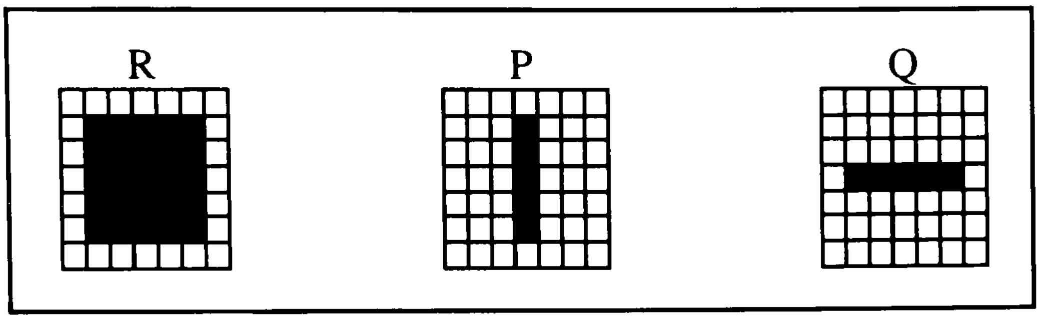

Figure 4.4. Fast implementation of a convex structuring element. $A \oplus R = (A \oplus P) \oplus Q$ and $A \ominus R = (A \ominus P) Q$ since $R = P \oplus Q$. A is any data set in 2-D.

Properties of dilation and erosion can also be used for fast implementation of morphological operations using non-convex structuring elements [15]. Figure 4.5 shows a rectangular non-convex structuring element R. This kind of a structuring element is frequently used in the implementation of the connectivity preserving filters.

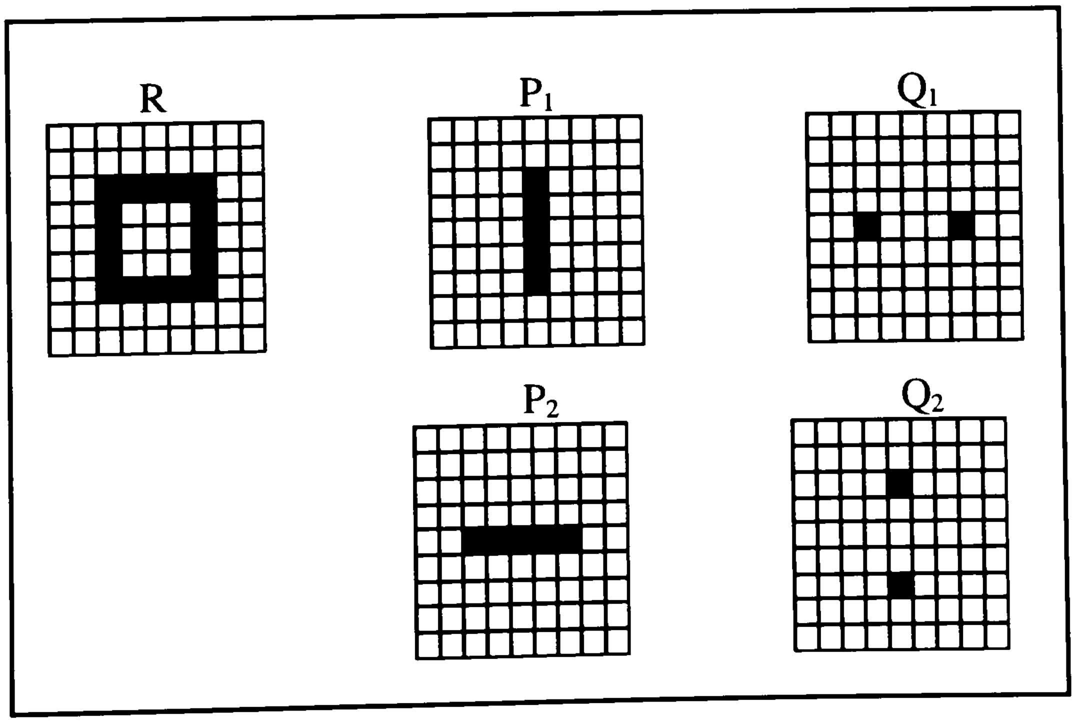

Figure 4.5. Fast implementation of a non-convex structuring element. $R = (P_1 \oplus Q_1) \cup (P_2 \oplus Q_2) \Rightarrow A \oplus R = ((A \oplus P_1) \oplus Q_1) \cup ((A \oplus P_2) \oplus Q_2)$, and $A \ominus R = ((A \ominus P_1) \ominus Q_1) \cap ((A \ominus P_2) \ominus Q_2)$. A is any data set in 2-D.

4.2 Median Filtering

The median filter was first introduced by Tukey in time series analysis in 1970. Later on, the median filter and its modifications found a variety of applications in the areas of digital image processing, digital image analysis, digital TV applications, speech processing and coding, etc. [3]. The main reason for the success of the median filter can be attributed to its computational simplicity and good performance [3].

In median filtering, the gray level of each pixel of the image is replaced by the median of the gray levels of the neighborhood of that pixel. This can also be thought of as replacing a pixel value by the median of the pixel values contained in a window around that pixel. That is,

$$v(m,n) = \text{median}\{y(m-k,n-l), \quad (k,l) \in W\}, \qquad (4.28)$$

where y(m,n) and v(m,n) are the input and output images, respectively, and W is a suitably chosen window. The algorithm for median filtering requires that the pixel values in the window be arranged either in an increasing or decreasing order. Then the median is determined by picking the middle value of the ordered set of pixel values [5]. Generally, the window size is chosen to be odd. However, if it is even, then the median is taken as the average of the two pixel values in the middle. Typically chosen window sizes are 3x3, 5x5 and 7x7 [5]. The principle behind the median filtering is to force points with distinct intensities to be more like their neighbors. This eliminates the intensity spikes that appear isolated in the area of the filter mask.

CHAPTER 5

PERFORMANCE EVALUATION CRITERIA

A set of standard criteria is needed to be defined in order to evaluate the performance of the filtering techniques. The quality of the filter can then be judged by either maximizing or minimizing a criterion. Therefore, it is desirable to have these criteria mathematically tractable. The equations that describe the performance evaluation criteria are described in this chapter.

5.1 Mean Square Error

For evaluating the quality of any processed image, the most commonly used measure is the mean square error (MSE). It is given by,

$$\mathrm{MSE} = \frac{\sum_{i=0}^{N-1}\sum_{j=0}^{M-1}\left(\hat{x}_{i,j} - x_{i,j}\right)^2}{\sum_{i=1}^{N-1}\sum_{j=0}^{M-1}\left(x_{i,j}\right)^2}, \tag{5.1}$$

where $\hat{x}_{i,j}$ and $x_{i,j}$ are the pixel intensity values at location (i,j) of the filtered and original image, respectively. N and M are the number of pixels in each row and column of the images, respectively.

5.2 Normalized Mean Square Error

A variation of the MSE is the normalized mean square error (NMSE). It is defined as,

$$\mathrm{NMSE} = \frac{\sum_{i=0}^{N-1}\sum_{j=0}^{M-1}\left(\hat{x}_{i,j} - x_{i,j}\right)^2}{NM * x_{max}^2}, \tag{5.2}$$

where $\hat{x}_{i,j}$, $x_{i,j}$, N and M are as described in section 5.1, and x_{max} is the maximum possible intensity value of the image.

5.3 Peak Signal-to-Noise Ratio

Here, the pixel value differences between the original (x) and the filtered ($\hat{x}$) images are considered as noise and a new measure of the NMSE is defined as the signal-to-noise ratio.(SNR). The peak signal value of a gray level image is usually taken as the highest gray level value, x_{max}. Hence, the peak signal-to-noise ratio in dB is defined as,

$$\mathrm{PSNR} = 10\log_{10}\frac{x_{max}^2}{\frac{1}{NM}\sum_{i=0}^{N-1}\sum_{j=0}^{M-1}\left(\hat{x}_{i,j} - x_{i,j}\right)^2} = 10\log_{10}\frac{1}{\mathrm{NMSE}}, \tag{5.3}$$

and the notations are the same as in section 5.2.

CHAPTER 6

RESULTS AND DISCUSSION

6.1 Speckle Reduction in a SAR Image

The original SAR image was decomposed as discussed in Chapter 3 by using Daubechies 4 and Daubechies 12 wavelet coefficients. Figure 6.1 shows a second level wavelet decomposition of the SAR image using Daubechies 12 coefficients (DAUB 12).

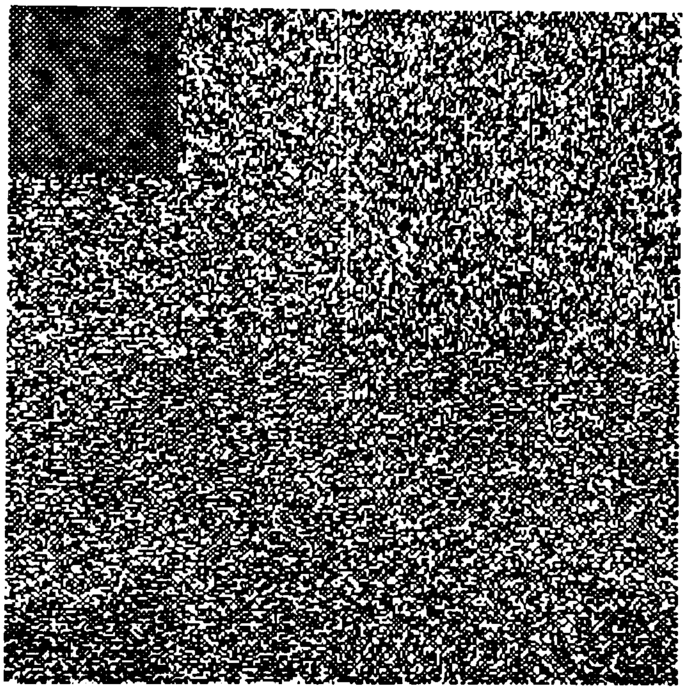

Figure 6.1. Second level wavelet decomposition of 256x256 SAR image using Daubechies 12 coefficients.

It is known that wavelet transforms decompose images into multiscale details. Speckle noise power is confined to small scales, and signal power at small scales corresponds to high frequencies in the wavelet domain. Thus, the three detail images of the wavelet decompositions of the SAR image were discarded, regarding them as representations of speckle noise frequencies. This procedure can be carried out for successive levels of decomposition, however, with some caution. As the level of decomposition goes high, the discarding of the detail images can destroy some of the relevant spatial information of the image. In the present work, this selective discarding of detail images was done for only two levels of decomposition.

The reconstructed images using both sets of coefficients showed a considerable reduction of noise. However, Daubechies 4 coefficients introduced a blocking artifact in the reconstructed image. Therefore, Daubechies 12 coefficients were chosen to implement the wavelet domain filter for speckle removal following the procedure previously described.

Connectivity preserving morphological filtering was performed on the SAR image by using the ASF technique based on bounded closing and bounded opening operators. Since the operations bounded closing and opening do not commute, different results were obtained when the order of closing and opening operations was switched in the ASF. However, previous work by Kher [15] shows that if the speckle image contains high density and high amplitude noise, then the close-opening operation performs better than the open-closing operation. It is also shown that open-closing tends to darken the image in such a situation. The SAR image we used was found to be corrupted by noise that satisfied these conditions. This is illustrated in Figure 6.2, which is an intensity profile of the SAR image along the 100th row. Therefore, ASF based on bounded close-opening operations was employed as the speckle reduction technique.

The connectivity preserving morphological filtering procedure is as follows. First, the SAR image was preprocessed with a standard close-opening operation using a

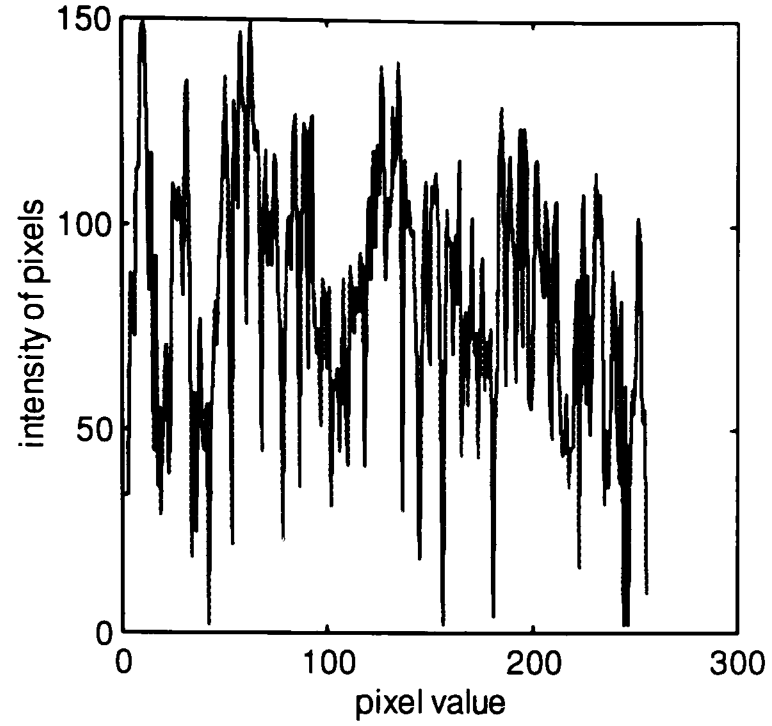

Figure 6.2. Intensity profile of SAR image at row 100.

2x2 rectangular structuring element. This was done in order to remove thin straight line elements in the image. Then, bounded close-opening was performed with a sequence of square structuring elements of sizes 5, 7, 9, 11, 13, and 15. The large sizes of structuring elements and their boundaries were implemented by using erosion and dilation properties of smaller structuring elements as described in Chapter 4.

A standard 3x3 Median filter was also implemented. Figure 6.3 shows the original SAR image. Figures 6.4 through 6.6 show the results of the original SAR image after wavelet filtering, median filtering, and connectivity preserving morphological filtering, respectively.

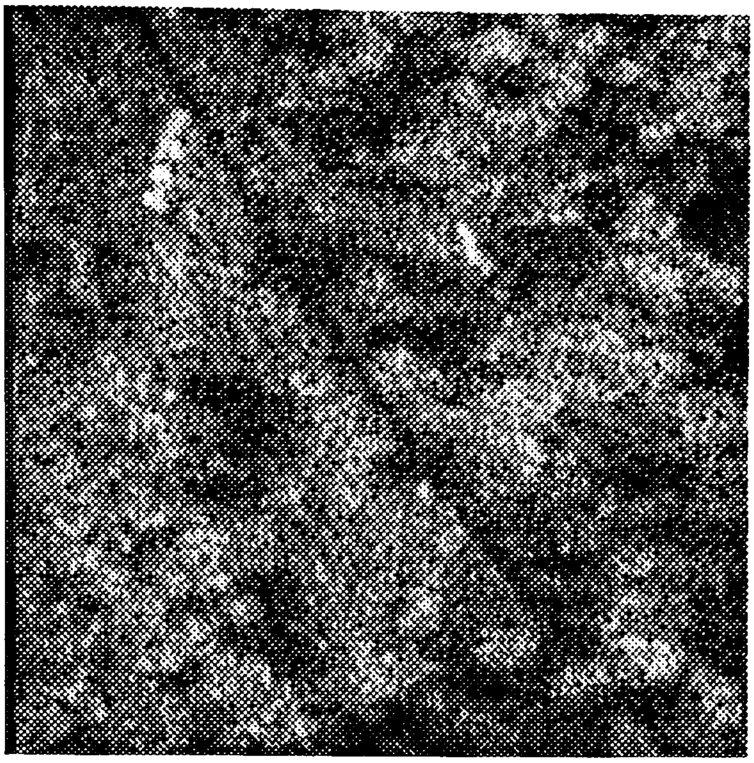

Figure 6.3. 256x256 8 bits/pixel original SAR image.

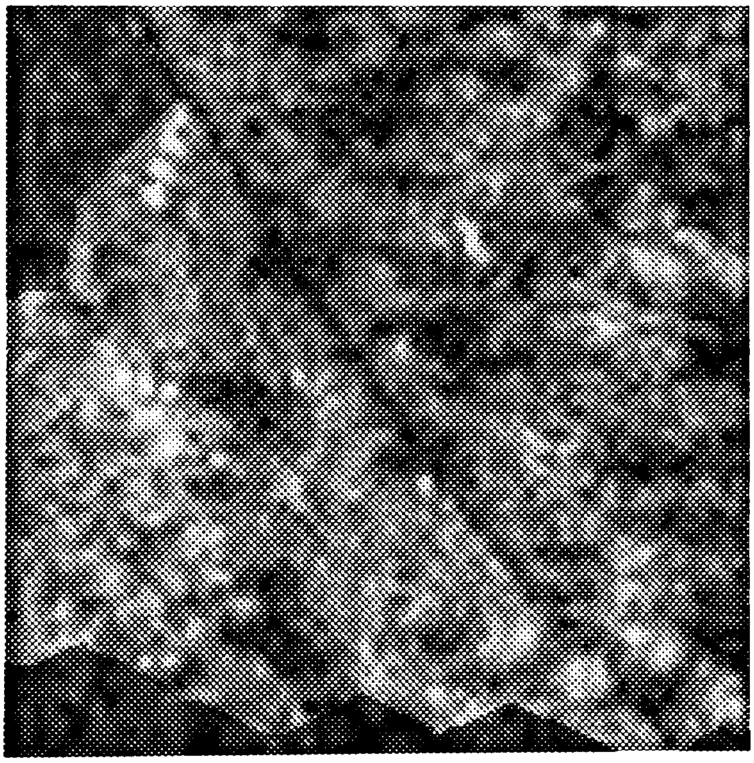

Figure 6.4. Original SAR image after wavelet filtering using DAUB 12.

Figure 6.5. Original SAR image after median filtering.

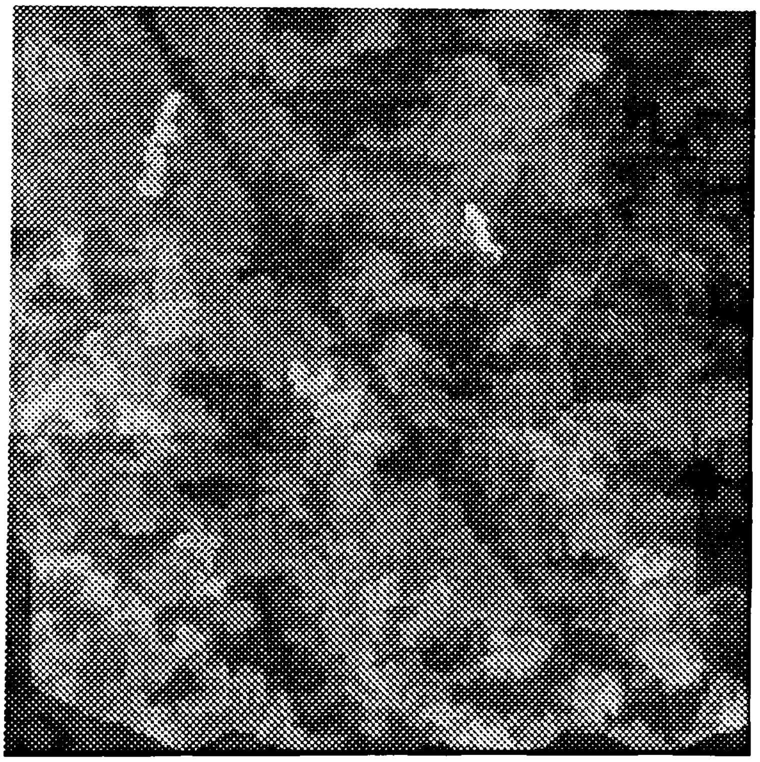

Figure 6.6. Original SAR image after connectivity preserving morphological filtering.

All three filters appear to have removed noise from the SAR image considerably. However, the wavelet filter has resulted in severe blurring of the image. The median filter has retained more information, but has destroyed some of the fractal details of the image. Among all three filters, the connectivity preserving morphological filter shows the best performance. It has resulted in an image with fine boundary details and fractal features.

6.2 Speckle Reduction in a Medical Ultrasound Image

The ultrasound image used in this work is a coronal view of the left kidney of a patient, and is shown in Figure 6.7. Due to the poor contrast, also depicted by the narrow histogram of Figure 6.8, the image was enhanced by a contrast stretching operation. Figures 6.9 and 6.10 show the histogram representation of the enhanced image, and the enhanced image, respectively.

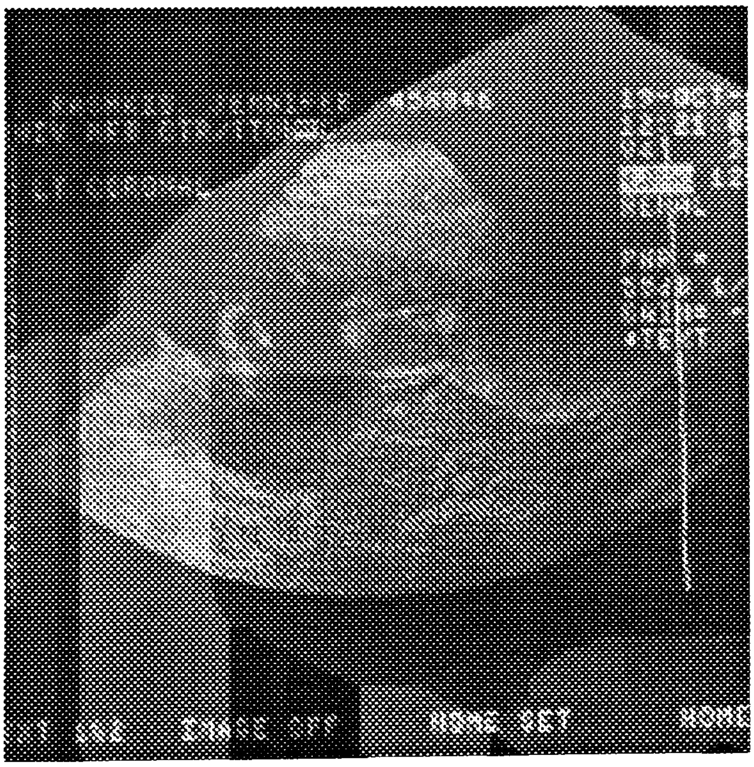

Figure 6.7. 256x256 8 bits/pixel original ultrasound image.

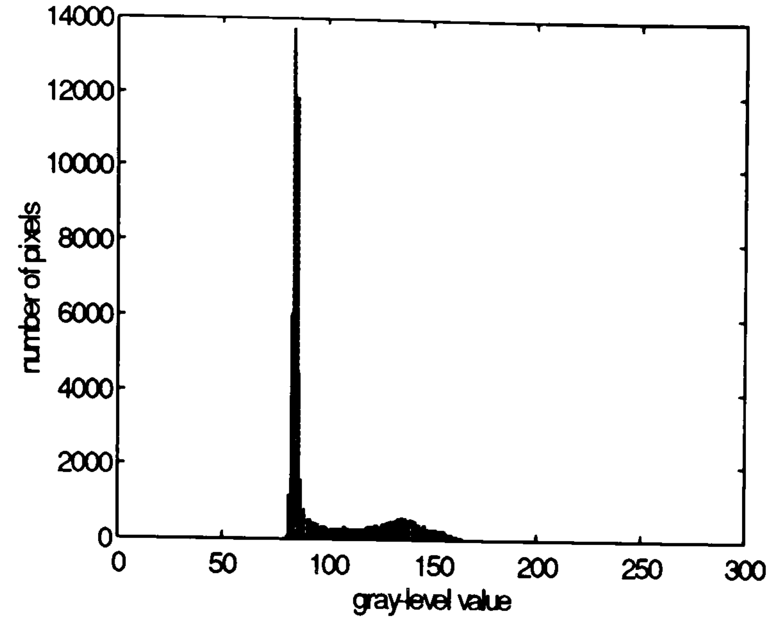

Figure 6.8. Histogram of the original ultrasound image.

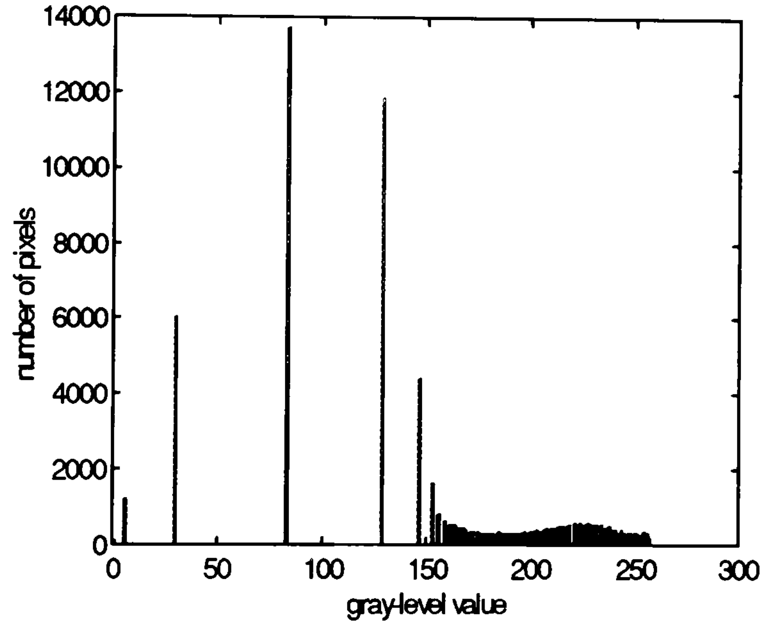

Figure 6.9. Histogram of the enhanced ultrasound image.

Speckle noise, simulated by using the multiplicative noise model described in Chapter 2 was then introduced to the enhanced image. Since speckle is a strong source of noise, the MSE of the noisy image with respect to the enhanced image was significantly large. Therefore, a noisy image with a reasonable MSE was generated by using the frame averaging technique described in Chapter 2. The number of frames used was 25.

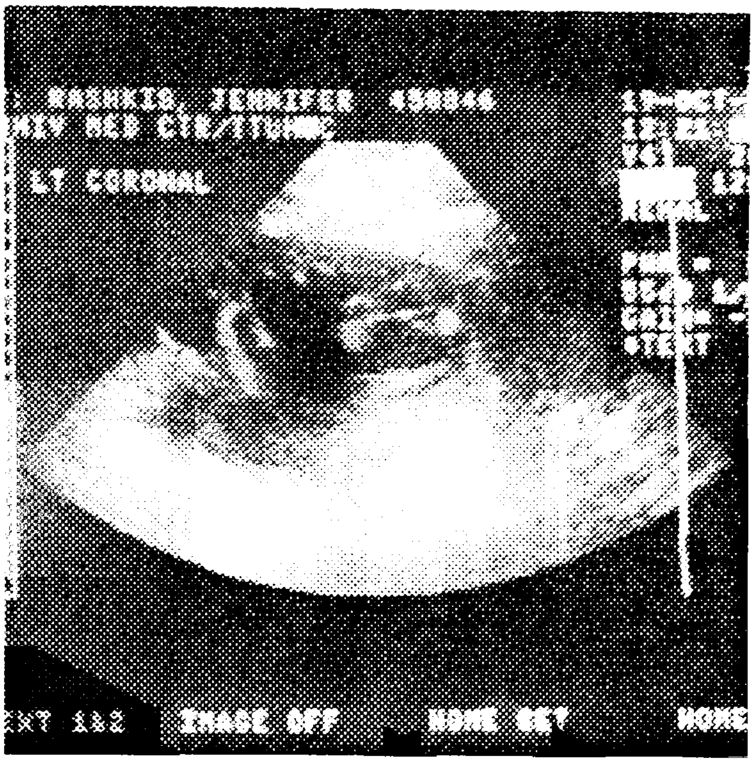

Figure 6.10. Enhanced ultrasound image.

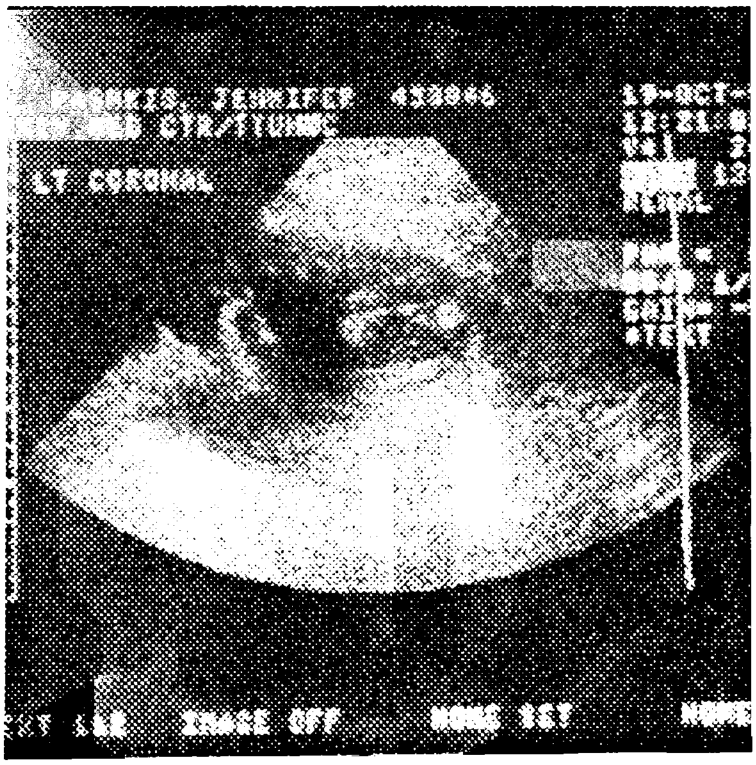

Figure 6.11. Enhanced image with simulated speckle noise.

Figure 6.11 shows the noisy enhanced ultrasound image that was used as the source image in the filtering processes. For wavelet filtering, DAUB 12 coefficients were used. The image was decomposed twice, and then all three detail images were discarded at each level. Median filtering of the image was performed by using a 3x3 mask. For the connectivity preserving morphological filtering, the ultrasound image was first preprocessed with a standard close-opening operation using a 2x2 rectangular structuring element. Then, bounded close-opening was performed with a sequence of square structuring elements of sizes 5 and 7.

Figures 6.12 through 6.14 show the results of the enhanced noisy ultrasound image after wavelet filtering, median filtering, and connectivity preserving morphological filtering, respectively.

Figure 6.12. Enhanced noisy ultrasound image after wavelet filtering using DAUB 12.

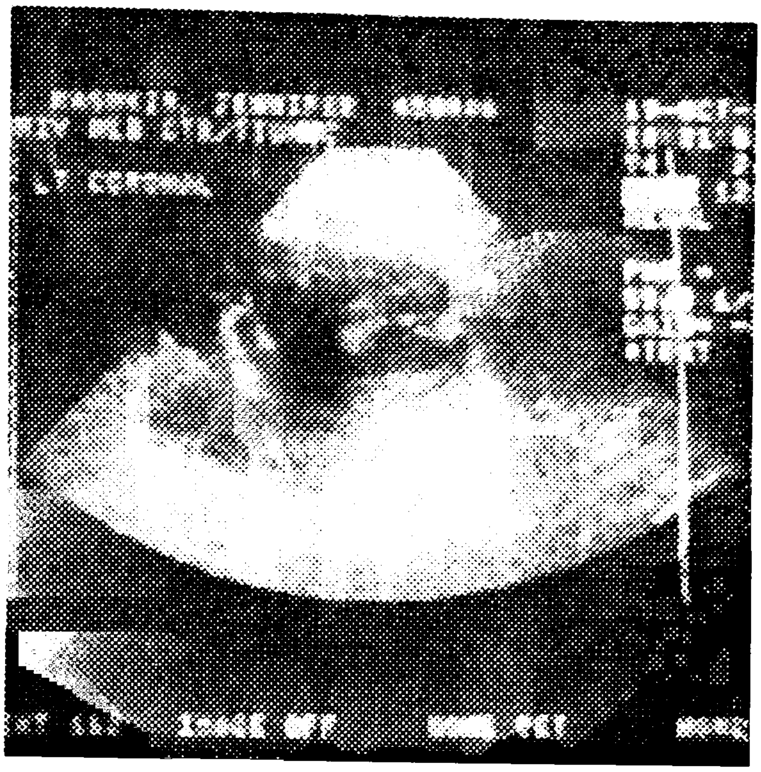

Figure 6.13. Enhanced noisy ultrasound image after median filtering.

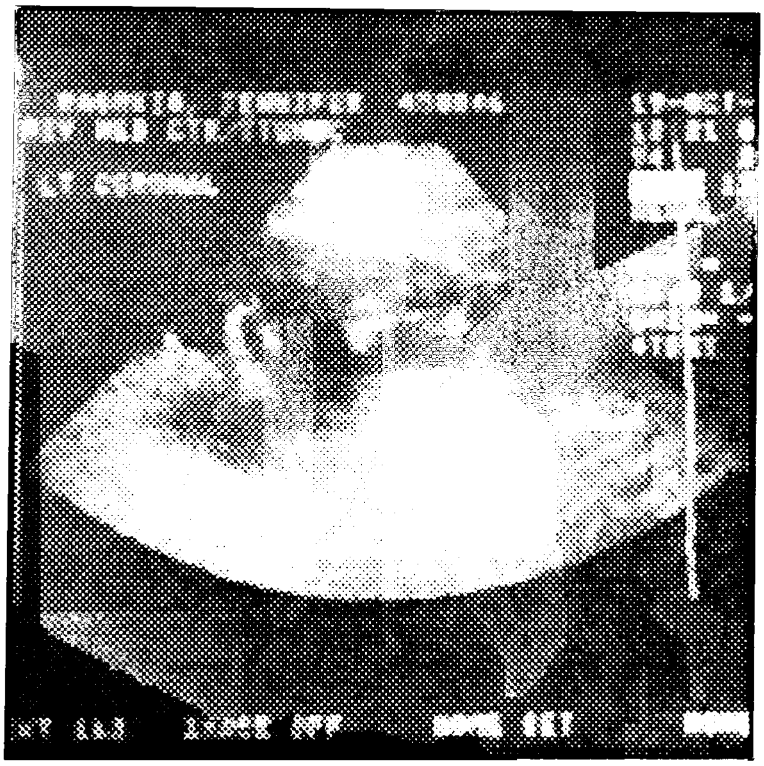

Figure 6.14. Enhanced noisy ultrasound image after connectivity preserving morphological filtering.

As in the case of speckle reduction in SAR images, all three filters appear to remove noise from the ultrasound image also, considerably. However, the wavelet filter has resulted in severe blurring of the image. The median filtered image shows a few speckle spots remaining and some distortion of the fractal details. The connectivity preserving morphological filter has resulted in an image with fine boundary details and fractal features and appears to be the best technique among all the three filters [22]. This is confirmed by the statistical criteria calculated as shown in Table 6.1.

Table 6.1. Performance of filters on enhanced noisy ultrasound image.

Filter Type	MSE	NMSE	PSNR
Wavelet	0.0489	0.0080	20.9585
Median	0.0658	0.0108	19.6644
Morphological	0.0325	0.0053	22.7343

Intensity profiles of the images were also analyzed in order to evaluate the performance of the filters. The 128th row of the enhanced noisy image was selected for the intensity profile analysis as shown in Figure 6.15. Figures 6.16 and 6.17 show the intensity profiles of the enhanced noisy and the enhanced ultrasound images, respectively. The intensity profiles of the wavelet, median and connectivity preserving morphological filtered images are illustrated in Figure 6.18 through 6.20, respectively.

Table 6.2 shows the MSEs of the line scans of the three filters. The connectivity preserving morphological filter shows the least amount of error in the mean square sense. Also, when the shape of the intensity profile of the enhanced image is compared with that of the filtered images, the connectivity preserving morphological filtered image gives the closest representation. Thus, we can further justify our conclusion of connectivity preserving morphological filtering performing the best in speckle noise removal compared to wavelet or median filtering.

Table 6.2. MSE calculations of line scans of filtered images.

Filter Type	MSE
Wavelet	0.0200
Median	0.0431
Morphological	0.0184

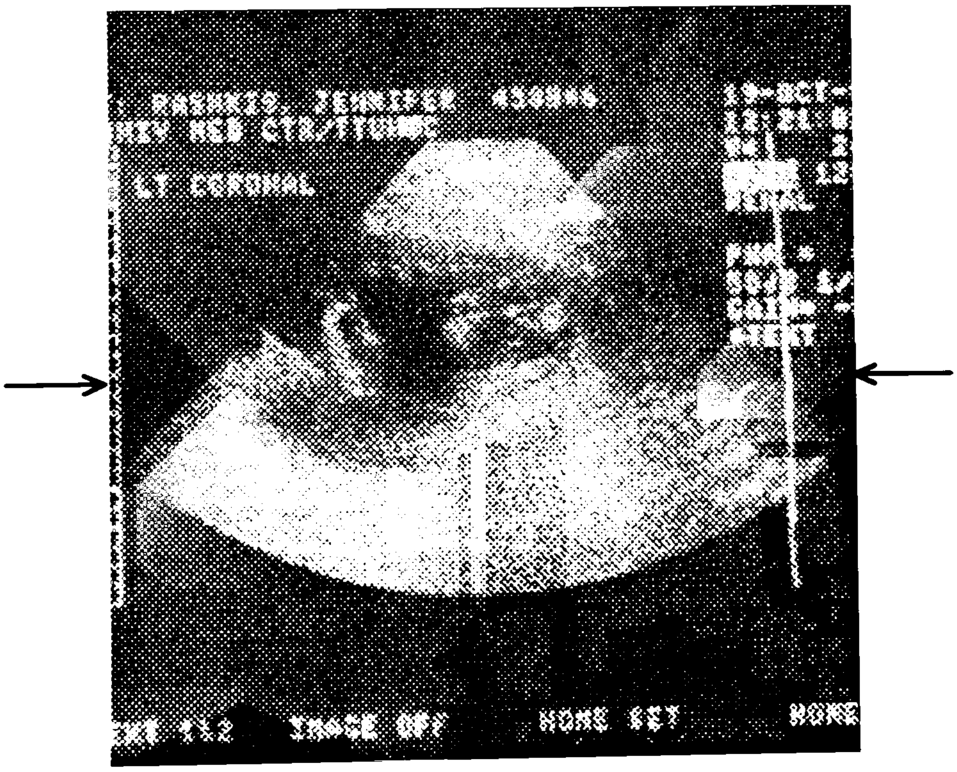

Figure 6.15. Enhanced noisy ultrasound image showing the selected row (128) for intensity profile analysis.

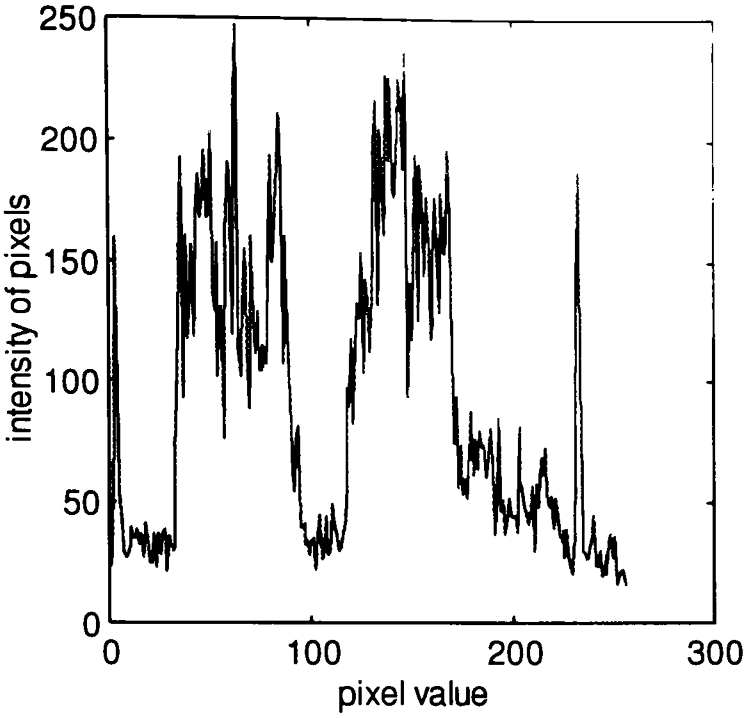

Figure 6.16. Intensity profile of enhanced noisy ultrasound image.

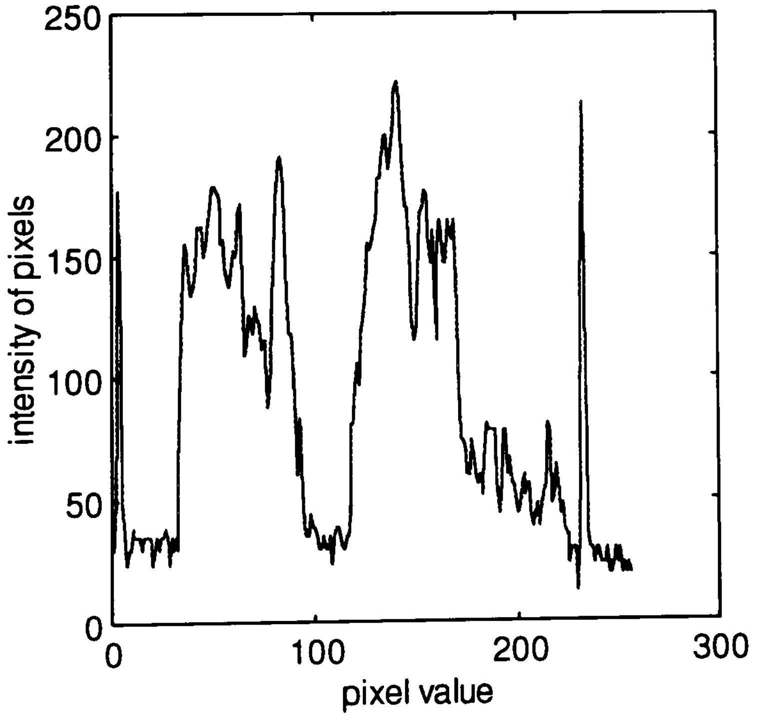

Figure 6.17. Intensity profile of enhanced ultrasound image.

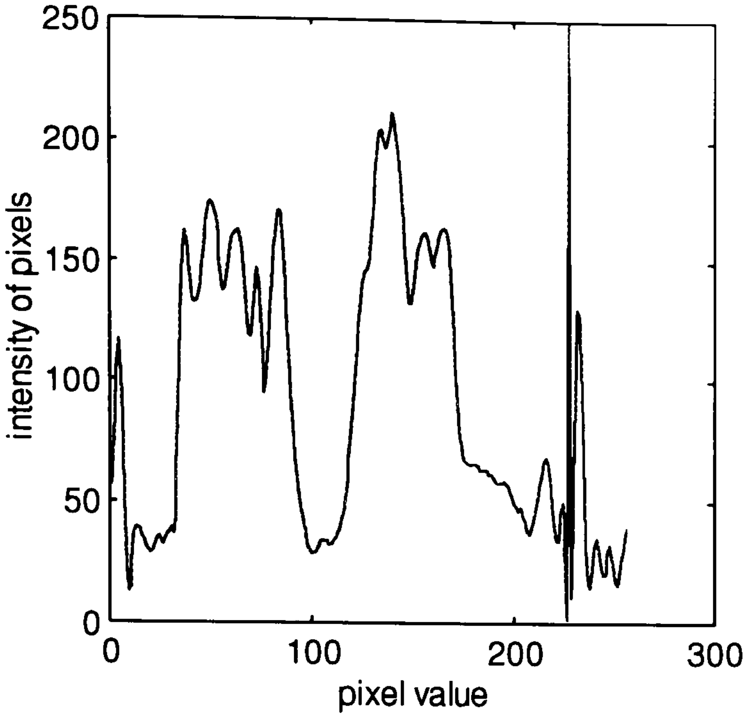

Figure 6.18. Intensity profile of wavelet filtered ultrasound image.

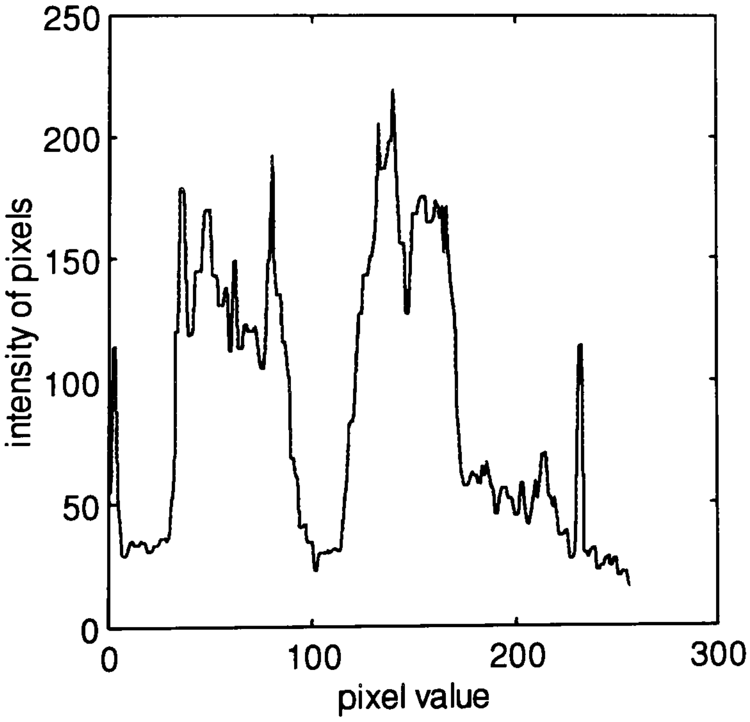

Figure 6.19. Intensity profile of median filtered ultrasound image.

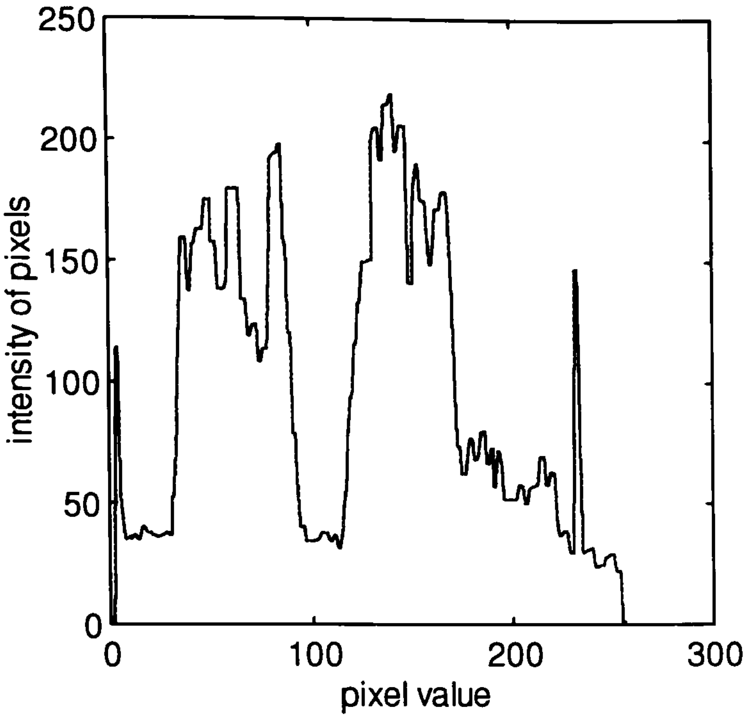

Figure 6.20. Intensity profile of connectivity preserving morphological filtered ultrasound image.

CHAPTER 7

CONCLUSIONS AND FUTURE WORK

This thesis has presented a comparison of the performance of linear and nonlinear filtering techniques in restoration of images corrupted by signal dependent speckle noise. The linear technique chosen was a wavelet transform-based filter, and the nonlinear methods chosen were conventional median and recently developed connectivity preserving morphological [15] filters. The results demonstrated a superior performance by the connectivity preserving morphological filter over the median and wavelet filters in preserving spatial details of images while removing speckle noise.

In the case of the wavelet transform domain filter, it was shown that the performance of the filter improved as the selected number of wavelet coefficients was increased. Yet, it blurred the edges of the images. Thus, this filtering technique presented a tradeoff between the SNR and the presence of small features in the filtered image. The features that were the same size as noise were also suppressed in the filtering process because they were not distinguished from the noise. The median filter, on the other hand, suppressed noise appreciably; however, it destroyed some fractal details of images.

The significance of the performance of the connectivity preserving morphological filter is that it preserved the microstructures of the images while removing noise. These structures often help in evaluating the information content in an image. There are several other advantages of using this filter as well. Morphological filtering is based on maximum and minimum operations as opposed to additions and multiplications used in linear filtering techniques. Consequently, the morphological filtering technique is faster than the linear filtering techniques. Also, it is performed in the spatial domain. Therefore, the results of morphological filtering can be directly interpreted in the spatial domain, which agrees with human intuition and perception of shapes and sizes.

An analytical investigation of the statistical properties of the connectivity preserving morphological filter is necessary to logically understand the principle of morphology and noise influences. Previous work by Wang et al. shows the statistical properties of both binary and multilevel, 1D and 2D, basic morphological operations [23]. Their results can be extended to analyze the statistical properties of the connectivity preserving morphological filter in the future.

Our work was primarily based on two digital images. A wide range of speckle images, such as echocardiographic images needs to be used to give a complete analysis of the performance of the filters. Finally, the filtered images need to be evaluated by professionals in the particular areas of application. Professional opinion on the quality of the image is critical since that is what ultimately determines the diagnostic information content in an image.

REFERENCES

[1] A.K. Katsaggelos, *Digital Image Processing,* Heidelberg, Germany, Springer-Verlag, 1991.

[2] H.C. Andrews and B.R. Hunt, *Digital Image Restoration,* Englewood Cliffs, NJ., Prentice-Hall, 1977.

[3] I. Pitas and A.N. Venetsanopoulos, *Nonlinear Digital Filters,* Norwell, MA., Kluwer Academic Publishers, 1990.

[4] D.T. Kuan, A.A. Sawchuck, T.C. Strand, and P. Chavel, "Adaptive restoration of images with speckle," *IEEE Trans. Accoust. Speech Signal Process.,* vol. ASSP-35, no 3, pp. 373-382, March 1987.

[5] Anil K. Jain, *Fundamentals of Digital Image Processing,* Englewood Cliffs, NJ., Prentice-Hall, 1989.

[6] L. Loupas, W.N. McDicken, and P.L. Allan, "An adaptive weighted median filter for speckle suppression in medical ultrasonic images," *IEEE Trans. Circuits Syst.,* vol. 36, no. 1, pp. 129-135, January 1989.

[7] J.S. Lim and H. Nawab, "Techniques for speckle noise removal," *Opt. Eng.,* vol. 20, no. 3, pp. 472-480, May-June 1981.

[8] Y. Qin, J. Dai, and J. Wang, "Recursive filtering technique for electronic speckle fringe patterns," *Opt. Eng.,* vol. 33, no. 5, pp. 1708-1711, May 1994.

[9] William B. Pennebaker and Joan L. Mitchell, *JPEG Still Image Data Compression Standard,* Van Nostrand Reinhold, New York, 1993.

[10] S. Mitra, R.A. Muyshondt, and S. Pemmaraju, "Hybrid high-fidelity image compression technique using multi-scale wavelets," *Proc. SPIE Wavelet Applications in Signal and Image Processing III,* vol. 2569, pt. 2, pp. 623-30, July 1995.

[11] Rubeena Shahnaz, *Image Compression in Signal-Dependent Noise,* Master's Thesis, Texas Tech University, 1995.

[12] T. S. McKechnie, "Speckle Reduction," book chapter in *Topics in Applied Physics:Laser Speckle and Related Phenomena,* edited by J.C. Dainty, vol. 9, Berlin, Germany, Springer-Verlag, 1975.

[13] Jong-Sen Lee, "Speckle analysis and smoothing of synthetic aperture radar images," *Computer Graphics Image Processing,* vol. 17, pp. 24-32, 1981.

[14] Y. Xu, J.B. Weaver, D.M. Healy, Jr., and J. Lu, "Wavelet transform domain filters: A spatially selective noise filtration technique," *IEEE Trans. Image Processing,* vol. 3, no. 6, pp. 747-757, November 1994.

[15] Alok Kher and Sunanda Mitra, "Optimum morphological filtering to remove speckle noise from SAR images," *Proc. SPIE Image Algebra and Morphological Image Processing IV,* vol. 2030, pp. 97-108, July 1993.

[16] J.W. Goodman, "Statistical Properties of Laser Speckle Patterns," book chapter in *Topics in Applied Physics:Laser Speckle and Related Phenomena,* edited by J.C. Dainty, vol. 9, Berlin, Germany, Springer-Verlag, 1975.

[17] M. Tur, K.C. Chin, and J.W. Goodman, "When is speckle noise multiplicative?," *Applied Optics,* vol. 21, no. 7, pp. 1157-1159, April 1982.

[18] Ali N. Akansu, "Wavelets and filter banks, a signal processing perspective," *IEEE Circuits and Devices,* pp. 14-18, Nov. 1994.

[19] Stephane G. Mallat, "A theory for multiresolution signal decomposition: The wavelet representation," *IEEE Trans. Pattern Anal. Machine Intell.,* vol. 11, no. 7, pp. 674-693, July 1989.

[20] Ingrid Daubechies, *Ten Lectures on Wavelets,* Society for Industrial and Applied Mathematics, Philadelphia, PA., 1992.

[21] Edward R. Dougherty, *An Introduction to Morphological Image Processing,"* vol. TT9, SPIE Optical Engr. Press, Bellingham, WA., 1992.

[22] S. Mitra, C. Wettasinghe, A. Kher, S. Pemmaraju, Y. Shieh, and G.H. Roberson, "Linear versus nonlinear model-based restoration of medical images corrupted with signal-dependent noise," *Proc. SPIE Image Processing,* vol. 2710, May 1996.

[23] Demin Wang, Veronique Haese-Coat, Alain Bruno, and Joseph Ronsin, "Some statistical properties of mathematical morphology," *IEEE Trans. Signal Processing,* vol. 43, no. 8, pp. 1955-1965, August 1995.

PERMISSION TO COPY

In presenting this thesis in partial fulfillment of the requirements for a master's degree at Texas Tech University or Texas Tech University Health Sciences Center, I agree that the Library and my major department shall make it freely available for research purposes. Permission to copy this thesis for scholarly purposes may be granted by the Director of the Library or my major professor. It is understood that any copying or publication of this thesis for financial gain shall not be allowed without my further written permission and that any user may be liable for copyright infringement.

Agree (Permission is granted.)

Student's Signature

04/23/96
Date

Disagree (Permission is not granted.)

Student's Signature

Date